Chapter 1 Electron Calorimeter

1.1 Overview

The Electron Calorimeter is designed to provide the event trigger for the experiment. This initiates data acquisition, in particular the readout of the tracker which provides the high resolution momentum measurement of the helical electron track. In addition, the calorimeter provides an energy measurement for the electron and a 3-dimensional position measurement for one point on the helical track. While the energy resolution does not compete with the momentum resolution of the tracker, it provides a measurement that is independent from the momentum reconstruction in the tracker.

The principal conclusion of the background studies of the MECO Physics Proposal is that, as in earlier experiments, electrons from muon decay in orbit (DIO) are the dominant source of background. In the free decay of a muon at rest to an electron and two neutrinos, the electron's energy is at most half the muon rest energy, but in the decay of a bound muon the energy approaches that of the conversion electron, ≅105 MeV, when the two neutrinos carry away little energy. In this limit, the electron recoils only against the nucleus, mimicking the two-body process that distinguishes muon to electron conversion. The spectrum (Figure 1-1) falls rapidly, as $(E_{max} - E)^5$ near the kinematic limit, but deviates from this form at lower energies. To eliminate the DIO background, good resolution in the measurement of the electron's energy is required. In MECO this is done in two steps: the calorimeter is used to minimize the number of DIO electrons that must be analyzed, while the tracker eliminates the bulk of the remainder of these events.

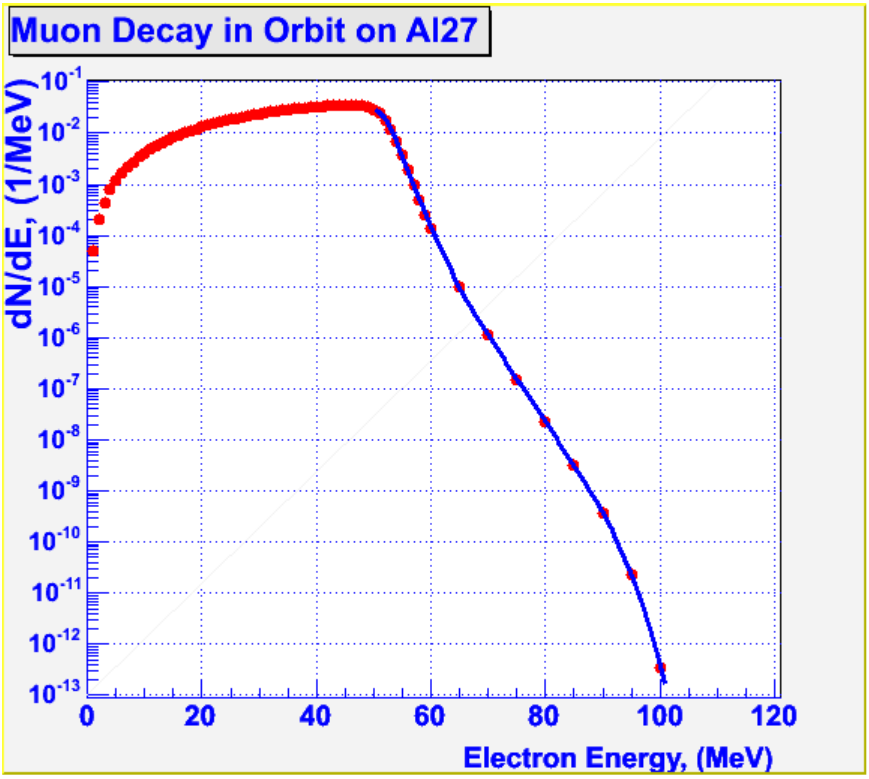

Figure 1-1: Differential energy spectrum for muon decay in orbit in Al.

However, the rapid rise of the DIO signal with lower energy is mitigated by the fall of the geometrical acceptance with lower energy, a feature that was an essential part of the experimental design; the detectors are built not to intercept electrons below about 50 MeV. Figure 1-2 shows the rapid fall off of the geometrical acceptance with decreasing electron energy, required to avoid the huge flux of decay electrons below 52.8 MeV.

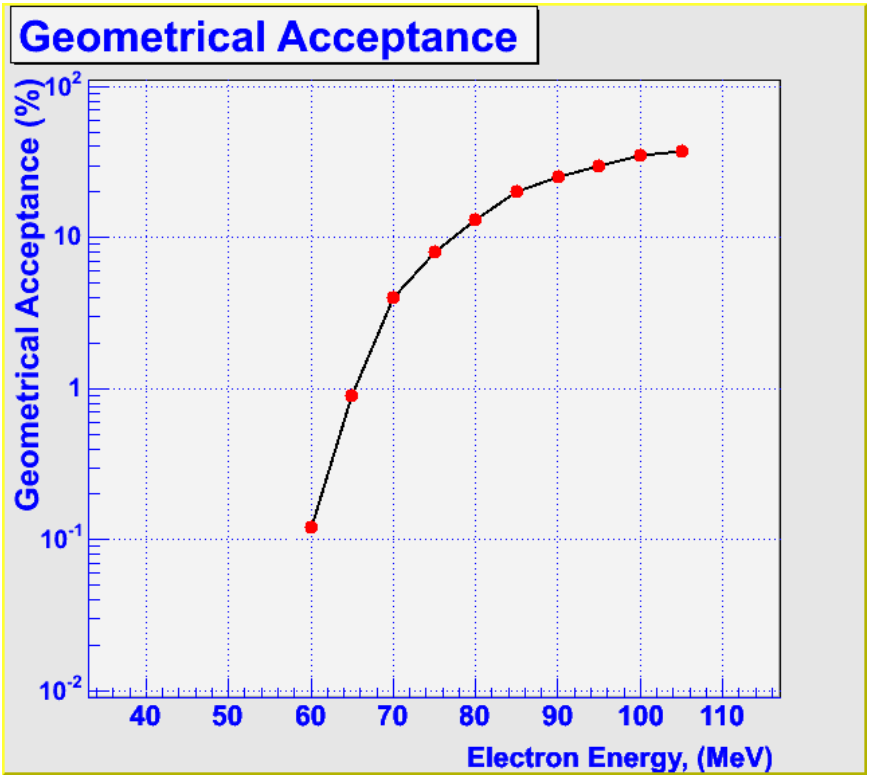

Figure 1-2: Fall-off in geometrical acceptance with decreasing electron energy required to reduce triggers from decay electrons.

Assuming that the resolution function is Gaussian, the probability of a DIO electron being measured to have an energy above a threshold E_{th} is given by

$$P = \int_{E_{th}}^{\infty} dE_M \int_{0}^{E_{max}} N(E) \cdot F_{geom}(E) \frac{1}{\sqrt{2\pi} \cdot \sigma} \cdot \exp\left(-\frac{(E - E_M)^2}{2\sigma^2}\right) dE$$

where N(E) is muon decay in orbit spectrum, $F_{geom}(E)$ is a geometrical acceptance of the calorimeter, E is a true electron energy, E_M is a measured electron energy, and E_{max} is a maximum electron energy equal to 104.963 MeV for an aluminum target. The probability of DIO contribution to calorimeter events {meco145} is shown in Figure 1-3 for different resolutions.

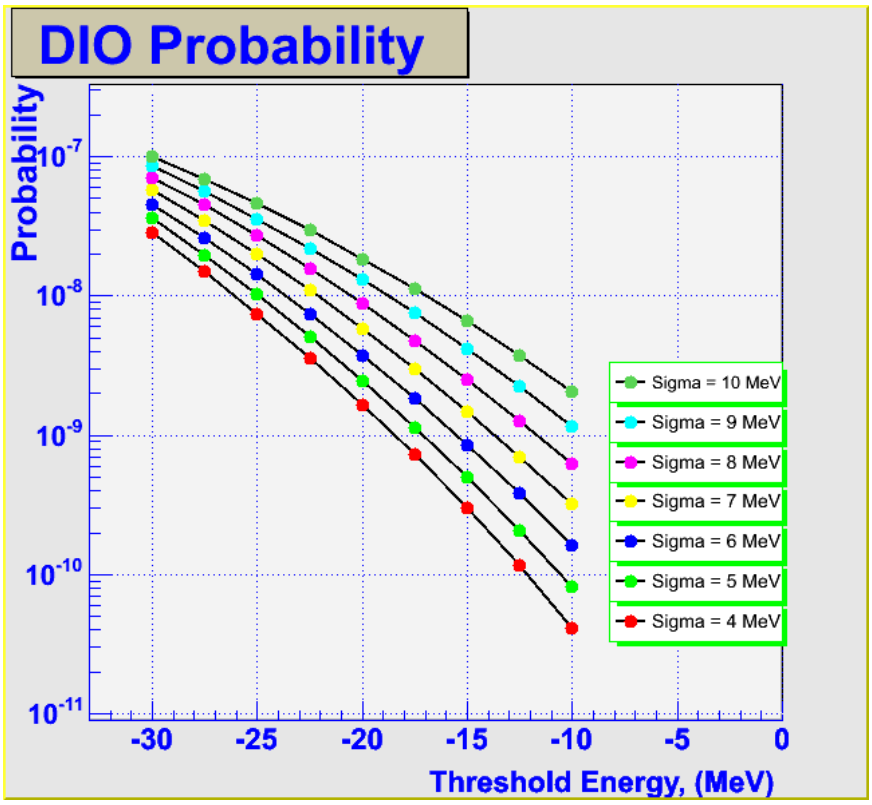

Figure 1-3: Probability of DIO contribution to a calorimeter events versus the threshold energy $\Delta = E_{th} - E_{max}$ measured from the endpoint for different resolutions. The effect of the geometrical acceptance has been folded in.

As can be seen in the figure, if the energy resolution of the trigger calorimeter is halved for the threshold energy E_{th} = 80 MeV, the trigger rate and final data sample size are reduced by a factor of 5. In these results the geometrical acceptance (see Figure 1-2) plays an important role suppressing the contribution from the electron spectrum below 70 MeV.

The expected number of DIO events in the calorimeter during the lifetime of the experiment can be estimated as

$$N = I_p \cdot \varepsilon_{\mu/p} \cdot \varepsilon_{gate} \cdot \left(1 - \varepsilon_{cap}\right) \cdot T \cdot P \,,$$

where I_p is an average proton flux 4×10^{13} /sec, $\varepsilon_{\mu/p}$ is a muon stopping efficiency in the Al target per primary proton 0.25% , ε_{gate} is a measured efficiency during the 650 nsec window, extending from 700 nsec to 1350 nsec after the pulse 50 %, P is a probability of DIO contribution events to a signal region above the threshold energy $\boldsymbol{\Delta}$ in the calorimeter (see Figure 1-3), ε_{cap} is a probability for a muon to be captured 60 % .

The calorimeter provides the trigger for the experiment. A lower threshold leads to many more false triggers in the data sample (Table 1.1) that must be reconstructed, without error, in the tracker. The additional triggers indeed come from lower energy electrons, for which the probability of confusion with an 105 MeV electron is small, but the number is much greater; there are 20 times as many decay electrons in the region above 80 MeV as there are above 90 MeV if the resolution σ = 5 MeV.

Table 1.1: Expected number of DIO events in the calorimeter for 10^7 sec. The energy-resolution and geometrical acceptance are included.

Threshold Energy (MeV)	75	80	85	90	95
Number of events (σ = 5 MeV)	7.2×10^9	2×10^9	5×10^8	1×10^8	1.7×10^7
Number of events (σ = 8 MeV)	1.4×10^{10}	5.4×10^9	1.8×10^9	5×10^8	1.2×10^8

The calorimeter also provides additional meaningful constraints on the event, ones that help directly with pattern recognition and lends credibility to any signal obtained from the tracker. The energy resolution can about 5% and an energy correlated (x, y, z) coordinate on the trajectory can be determined to about 1.5 cm (RMS). The event topology and the high crystal density makes possible a large acceptance for conversion electrons, 80%, while the acceptance for neutrals is just 14%, reducing the rate from gammas and neutrons that reach the detector directly from the muon target.

1.2 Crystal Choice and Detector Geometry

Table 1.2 gives the properties of a variety of crystals that have some appeal for use in high-energy experiments. In our application, a high rate environment with a pulsed beam producing a large "flash" of particles every 1.35 microseconds from which the detector must recover before the observation window starting some 600 nanoseconds later, there is need for a short scintillation decay time constant, short radiation length (dictated by the MECO geometry described below), relatively reasonable cost, and sufficient light yield at our low energy of 100 MeV.

Table 1.2 : Properties of Scintillating Crystals. Measured light yields vary greatly depending on dopant concentration, crystal quality, and the accuracy of corrections for light collection efficiency and detector quantum efficiency. Consistent comparisons to the literature for GSO, BGO, and $PbWO_4$ are achieved if the relative yields in the table are normalized to ~5 $\times 10^4$ photons/MeV for NaI(Tl).

Crystal	GSO (Ce)	BGO	CWO	CeF_3	BaF2	$PbWO_4$	CsI	CsI (Tl)	LSO	NaI (Tl)
Density, gm/cm^3	6.71	7.13	7.90	6.16	4.89	8.28	4.53	4.53	7.40	3.67
Rad.Length, cm	1.38	1.11	1.06	1.68	2.06	0.89	1.86	1.86	1.14	2.6
Decay Con.,ns fast slow	 30-60 600	300	5000	 8 20	 0.6 620	 ≤15 100	 10 1000	 1000	 12 47	230
Light Yield, rel fast slow	 20 2	10	30-40	 4 4	 5 16	 0.7 0.007	 4 4	 80	 ? 50-75	100
Peak λ fast slow	 430 430	480	480	 300 340	 210 310	440	 305 560	 560	 420,460 420,460	415
Temp. Coeff. % =°C		-1.6		0.14	-2/0	-2				~0
Rad Hard. (rad)	$>10^8$	10^{5-6}		10^{6-7}	10^{6-7}					10^3

We have made the choice of lead tungstate, $PbWO_4$, for the electron calorimeter. This choice, and our own laboratory studies leading to it, were inspired by the rapid progress made by the CMS Collaboration and their industrial partners in developing lead tungstate scintillating crystals for use in very high energy calorimetry at the LHC. The high density with a radiation length of 0.89 cm and short scintillation decay time of less than 15 ns make $PbWO_4$ very favorable for this application. The one difficulty with this crystal, a low light output (15 times less than BGO) was a concern for the low energy, 100 MeV application. However, in our lab tests this problem was overcome by:

- Cooling the crystals to -24^0 C. This increases the light yield of $PbWO_4$ by a factor of 2.3. At this temperature the scintillation decay also increases to about 25ns, still comfortable for the pulsed, gated application.
- The recent development by several companies, Applied Photonics, RMD, and Hamamatsu, of large area Avalanche Photodiodes of 1 to 2 cm^2, increasing the light collection significantly.
- The readout of a crystal by 2 APD's to further increase the light yield and also solve the APD Nuclear Counter Effect: a charged particle in the APD will produce a very large output signal which could be misinterpreted as high energy from the calorimeter. Comparison of the two APD amplitudes allows the rejection of these spurious signals.
- Our investigations with potential vendors, and the experience of CMS, ALICE and BTeV, indicate that $PbWO_4$ crystals can be made in the needed quantity at an acceptable cost.

Along the way we had examined several other scintillator choices. BGO has a very favorable light yield, reasonably short radiation length, but an unsuitably long decay time of 300ns. Crystals made from GSO or LSO, although not quite as dense, might be more suited to our application in other respects and would be the better choice. The light from these crystals has shorter decay time by an order of magnitude, is 2 – 3 times greater than the light from BGO, and at least 30 times greater than that from $PbWO_4$. The use of these crystals would result in considerably better resolution, but inquiries into obtaining GSO, for example, have led to the conclusion that the cost is far too high and a substantial production run to make the required number of crystals is currently unlikely. Two crystals with substantial light output and sizeable fast components are CeF_3 and pure CsI. There is no slow component in the light output from CeF_3. The light output of cesium iodide has a substantial 1 μs component that would probably have to be filtered out in this high rate application [118]. For both of these, their longer radiation length in the 1.7- 1.9 cm range , makes them less attractive in the proposed geometry.

The electron calorimeter consists of 4 vanes, each a high density bar that functions as a total absorption calorimeter. As shown in Figure 1-4, the bars are separated by 90° in azimuth, located at 3, 6, 9, and 12 o'clock. The active region of each bar extends radially from r = 39 cm to r = 69 cm, to match the active region of the tracker that is upstream of it.

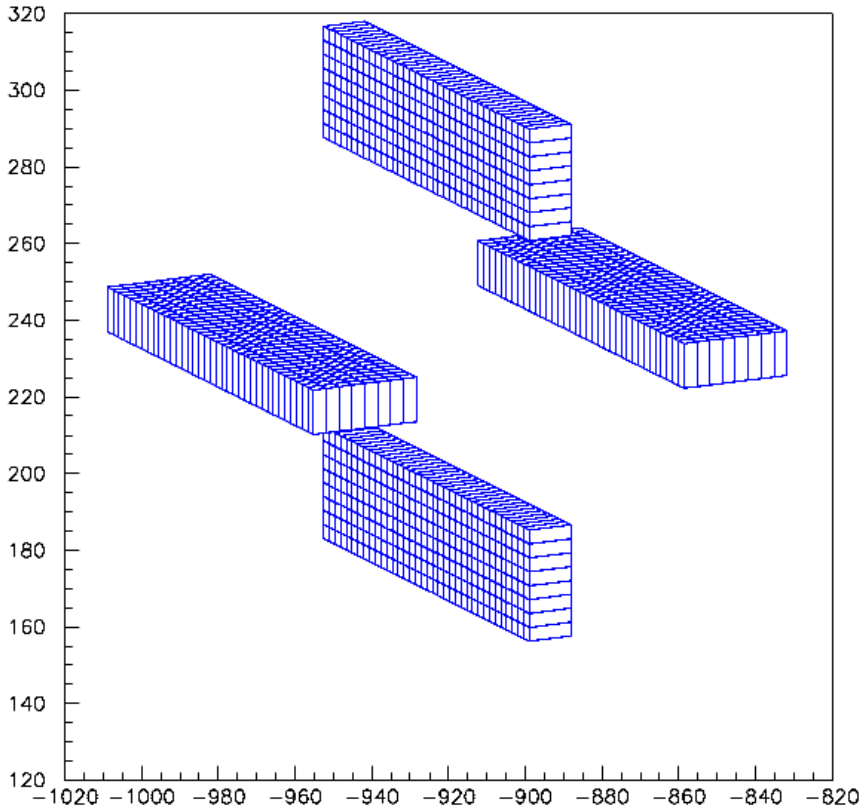

Figure 1-4 Crystal calorimeter. The four vanes consist of crystals 3.75 cm × 3.75 cm on a side and 12 cm in depth.

The length of the calorimeter along the beam, and its depth for containing the electron showers were selected by a Monte-Carlo simulation of the detector acceptance, with results shown in

Figure **1-5**. Based on this figure, a depth of 12cm (13.5 radiation lengths; ~18 r.l. for a typical incidence angle of 45^0) and a length of 120cm along the axis of the solenoid, the *z*-axis, were chosen as a reasonable compromise between cost and acceptance. The spiraling electrons strike one, but not both, of the 120 cm × 30 cm surfaces and are absorbed in the 12 cm thick calorimeter. The individual calorimeter cells are $3.75 \times 3.75 \times 12$ cm^3 crystal cell, with the transverse dimension a good match to the $PbWO_4$ Moliere radius of 2.2 cm. With the chosen dimensions, the number of crystal cells in each vane is 256 for a total count of 1024 crystals read out by 2048 APD's.

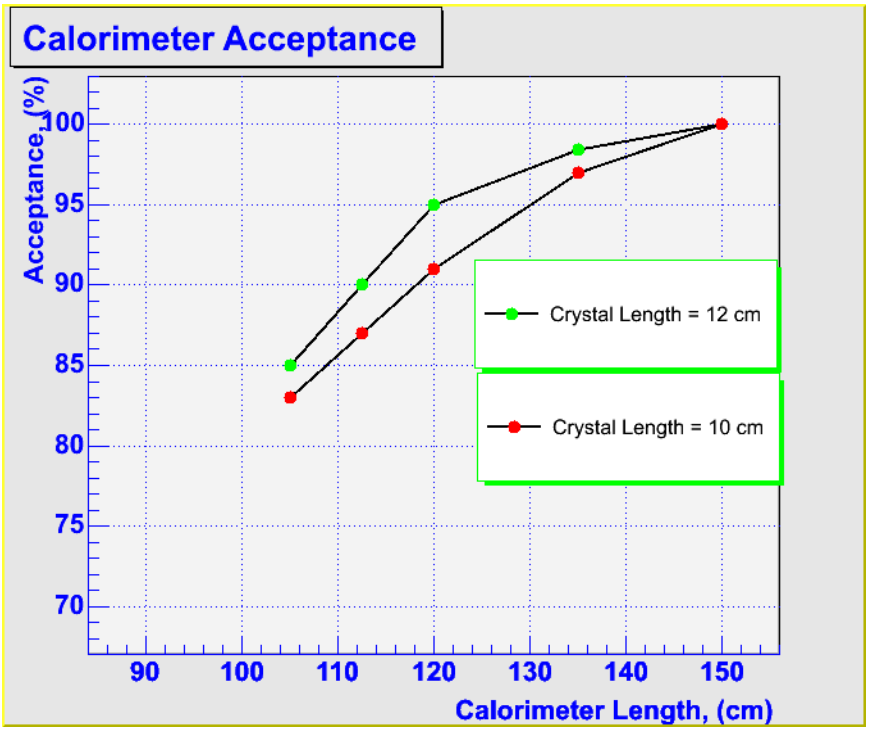

Figure 1-5: Relative acceptance vs. calorimeter length for two different depths, for an 80 MeV threshold. The curves are normalized to the acceptance at 150cm, a length corresponding to a full turn of the helical trajectory for a typical electron.

1.3 Detector Efficiency and Coordinate Resolution.

The four-vane geometry was studied using a full GEANT simulation of the detector. Electrons of 105 MeV were generated in the aluminum target and traced through the tracking detector to the electron calorimeter, which extends from 5.7 to 6.9 m from the end of the muon target. Only 'good' electrons, those producing quality tracks in the tracking detector, were retained for the calorimeter study. In Figure 1-6, the reconstruction efficiency of the detector is plotted as a function of the threshold imposed on the reconstructed energy. In the studies, electrons are considered only if they make total energy deposition in the calorimeter above some low threshold 10 MeV. A high energy-threshold can be imposed using the crystal calorimeter, eliminating the need to track low energy electrons from muon decay in orbit.

The crystal calorimeter geometry permits the reconstruction of three coordinates of the particle position at the calorimeter entry, independently of the tracker. To estimate the detector coordinate resolution, the cell energies obtained from a GEANT simulation were projected onto the radial, *x* or *y*, and *z* axes. An energy weighted sum of the coordinates of the centers of the struck cells was used to estimate the impact coordinate of the electron at the surface of the calorimeter. The coordinate resolution, using a center gravity method, is 1 cm and 1.5 cm RMS for z and radial (x or y) coordinate respectively. The resolution in the radial coordinate is worse because of shower leakage from hits near the edges of the bar, which is not as significant in the measurement of the *z*-coordinate. The resolution in the radial coordinate can be improved using the shower profile. It is clear that this well measured position, correlated with the energy deposition in the trigger calorimeter, provides a valuable constraint on the event.

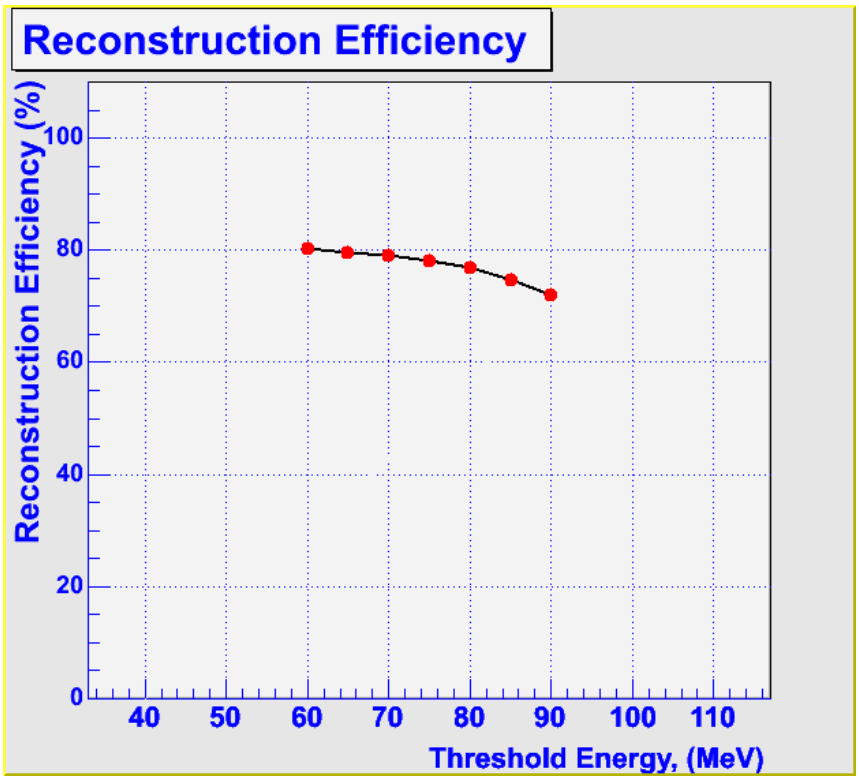

Figure 1-6: The calorimeter reconstruction efficiency versus threshold energy

1.4 Energy Resolution

The location of the trigger calorimeter in a 1 T magnetic field, the large initial high-rate flash before each data acquisition window, and severe time constraints imposed by the beam microstructure provide the major challenges to obtaining good energy resolution in the calorimeter. The 1 T field makes it difficult to take advantage of the broad bandwidth, high gain and low noise of photomultiplier tubes in this application. To overcome the magnetic field problem, many experiments have turned to sensing the light from the crystal using avalanche photodiodes, sometimes coupled in a creative fashion to the crystal {Lorenz:1986}. The high quantum efficiency of these devices and the stability achieved when they are coupled to a charge sensitive amplifier are advantages not shared by photomultiplier tubes. The down side is that electronic noise is introduced in sensing and amplifying the diode photocurrent, due primarily to the thermal noise associated with the channel resistance of the field effect transistor commonly used at the input stage of the amplifier. This series noise is largest when short shaping times in the amplifier-filter network are necessary, and it adds an energy independent component to the fluctuations in the diode dark current that particularly affects resolution at low energy.

There are contributions to the electron resolution from several sources, namely the energy deposition, electronic noise, photo-statistics, and pileup background fluctuations. These will be examined in turn.

1.4.1 Energy Deposition

The spectrum of energy deposited in the calorimeter shown in Figure 1-7, is visibly non-gaussian, has a full width at half maximum of 4 MeV and a long low energy tail from energy leakage, particularly for hits near the radial edge of the detector.

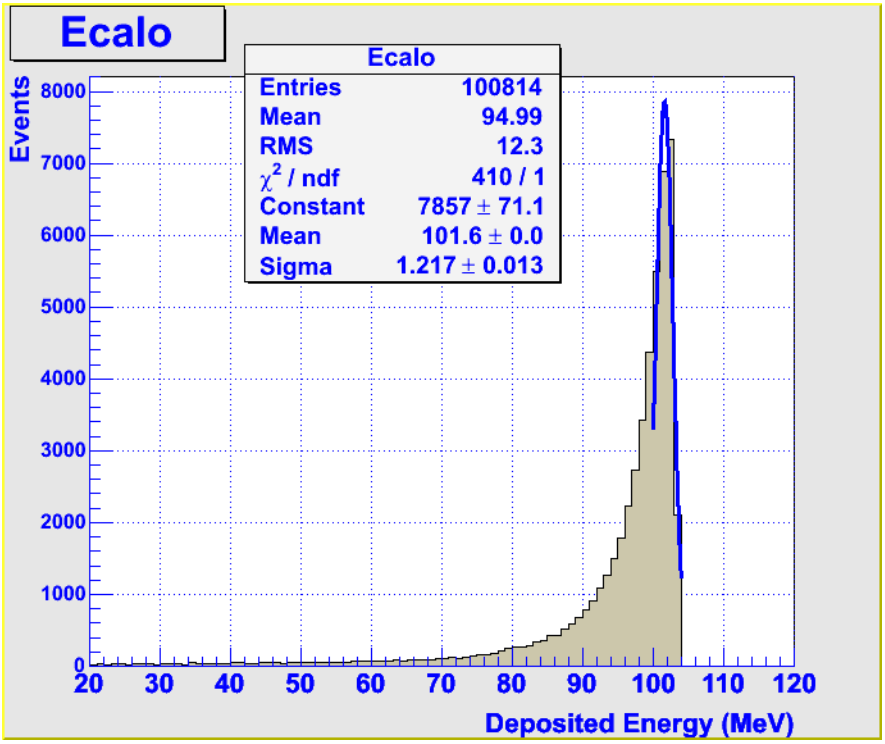

Figure 1-7: Energy deposited in the crystal calorimeter from a GEANT simulation; bin size is 1 MeV.

The energy deposited in the calorimeter is shared among many individual crystal cells. The distribution of the number of cells hit, with a mean of about 7, but extending up to 14, is shown in Figure 1-8 . It is the task of the calorimeter reconstruction in software to combine the information from the hit cells into an optimized calorimeter resolution.

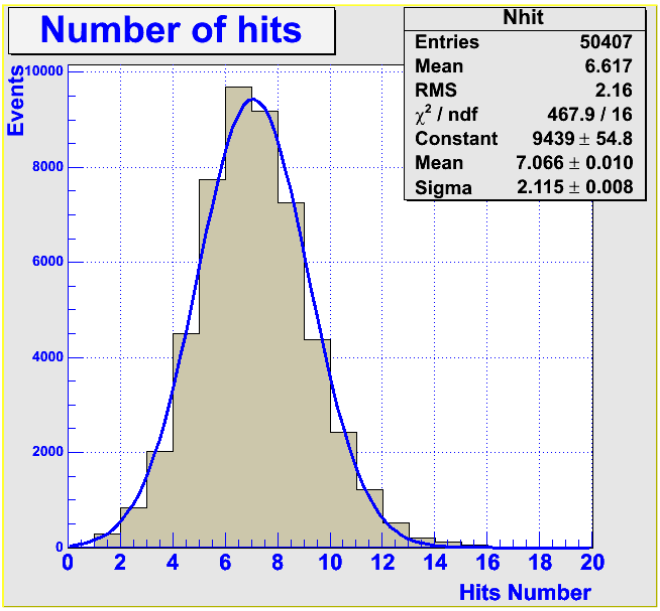

Figure 1-8: Number of cells in μ-e event with energy deposition greater than 1 MeV.

To the above energy deposition spread must be added the resolution contributions from other sources. The resolution is often described by the quadrature sum of three contributions:

$$\sigma(E) = A \oplus B\sqrt{E} \oplus CE \ .$$

The first term is the contribution from electronic noise and the second is due to photoelectron statistics. The third term, proportional to the energy E, includes several effects: intercalibration errors, non-uniform light collection over the crystal, fluctuations due to energy leakage, and, if not monitored effectively with time, collective temperature and gain drifts. Sometimes a fourth empirically observed term is included, proportional to $E^{1/4}$ and of order 1%.

1.4.2 Electronic Noise

Great progress has been made recently in using crystal calorimeters at low energy. The development of large area photodiodes with large depletion depths, and therefore small capacitance, has been important in improving the signal-to-noise ratio at low energy {Kubota:1992}{Barlow}. Avalanche photodiodes (APD's), typically with gains of 100 – 200, can be used to reduce the series noise or to achieve smaller shaping times.

The first term in the expression for σ(E) is often most difficult to limit at low energy when using photodiodes. The quantity A in the equation above is called the equivalent noise energy and is the ratio of the equivalent noise charge, expressed in units of the electron's charge, to the light collected, L, in photoelectrons per MeV. Figure 1-9 shows the equivalent circuit used in this analysis to calculate the noise level from an APD connected to a $PbWO_4$ crystal. The current I_{in} is the signal current after amplification by the photodiode gain M and e_s is the noise associated with the series resistance of the diode, expressed in units volts/$\sqrt{Hz}$. The RMS fluctuation in the dark current of the photodiode i_n, with surface I_s and bulk I_B contributions, is

$$i_n = M\sqrt{2e(I_s / M^2 + FI_b)}\,, \quad (\mathrm{M} = 200, \quad I_B \approx 10\ \mathrm{nA})$$

in units of $\mathrm{A}/\sqrt{\mathrm{Hz}}$. The symbol F is the excess noise factor,

$$F = 1 + \frac{\sigma_M^2}{M^2}\,,$$

that originates from fluctuations in the gain M, and also results in an increase in the photostatistics error

$$\sqrt{\frac{1}{N_e}} \Rightarrow \sqrt{\frac{F}{N_e}}\,,$$

where N_e is the number of electron-hole pairs generated in the diode. The diode capacitance C_d and the FET input capacitance C_i are also shown, as well as the thermal noise contribution from the FET channel resistance e_n. Table 1.3 summarizes the values of the parameters used in the present exercise. They are very device dependent.

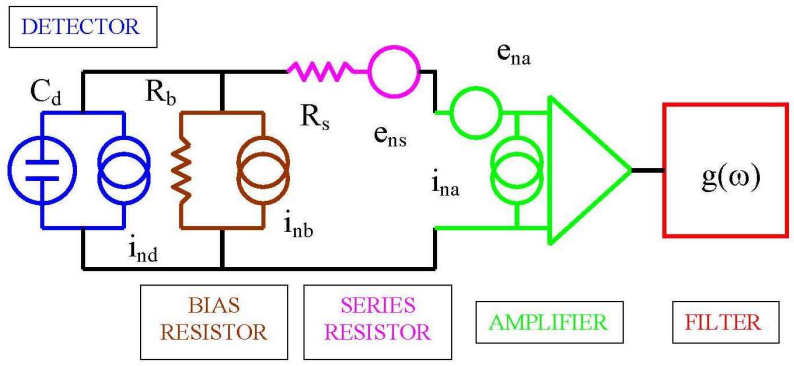

Figure 1-9: Equivalent circuit used in simulation of electronic noise.

The equivalent noise energy is obtained by setting the signal equal to the RMS noise voltage,

$$V_{signal} = \frac{Q}{C_f} F(t_{\max}) = V_{rms}$$

where $F(t_{max})$ is the response of the circuit to the input from the scintillation light at its maximum, the time it is sampled t_{max}. The scintillation decay time of the is included in F(t) as a single exponential, with the time constants 25 nsec. The total charge Q is given by Q = E x L x M x e, where E is the electron energy in MeV, L is the electron yield in e's per MeV, M is an APD gain, e is an electron charge.

The result is

$$ENE = \frac{1}{eLF(t_{\max})}\left[\frac{e_T(C_d + C_i)}{M\sqrt{\tau_s}} \oplus \sqrt{\tau_p}\,\frac{i_n}{M}\right].$$

In this equation, the times τ_s and τ_p are obtained from the filter transfer function g(ω) through the series and parallel noise integrals

$$\tau_s^{-1} = \int_0^\infty g(\omega)^2 \frac{d\omega}{2\pi}, \qquad \tau_p = \int_0^\infty \frac{g(\omega)^2}{\omega^2}\frac{d\omega}{2\pi}, \qquad e_T = e_s \frac{C_d}{C_d + C_i} \oplus e_n$$

where e_n is a noise of the preamplifier input FET transistor , e_s is an equivalent noise from the APD series resistance.

In the equivalent noise energy, i_n/M is approximately independent of *M*. The equation indicates that the ENE coming from the series noise (the first term) is reduced by a factor of *M* compared to a PIN diode of similar properties. This is not surprising because the noise source is the FET channel resistance after the APD.

Table 1.3: Parameters used in calculation of the electronic noise with Avalanche photodiodes.

Parameter	Device	Value
$e_n(nV/\sqrt{Hz})$	BF861A	1.0
C_{gs} (pF)	BF861A	≤10
C_d (pF)	RMD APD	130 pF *V* = 1.6 kV
I_b (nA)	RMD APD	10 nA *M* = 200
R_s	APD	30 ohms
Excess Noise *F*	APD	2.2
Diode Area	APD	1.7 cm^2
L e's/(MeV · diode)	$PbWO_4$(cooled)	19
Scint. Decay (nsec)	$PbWO_4$(cooled)	25

Figure 1-10 shows the equivalent noise energy and the error (in MeV) resulting from fluctuations in the number of electron-hole pairs made in the APD for $PbWO_4$ with 2 APD's and with crystal () and diodes cooled to -20 C. The contributions to the resolution from these two sources are plotted as a function of the RC time constant for a CR – $(RC)^2$ filter.

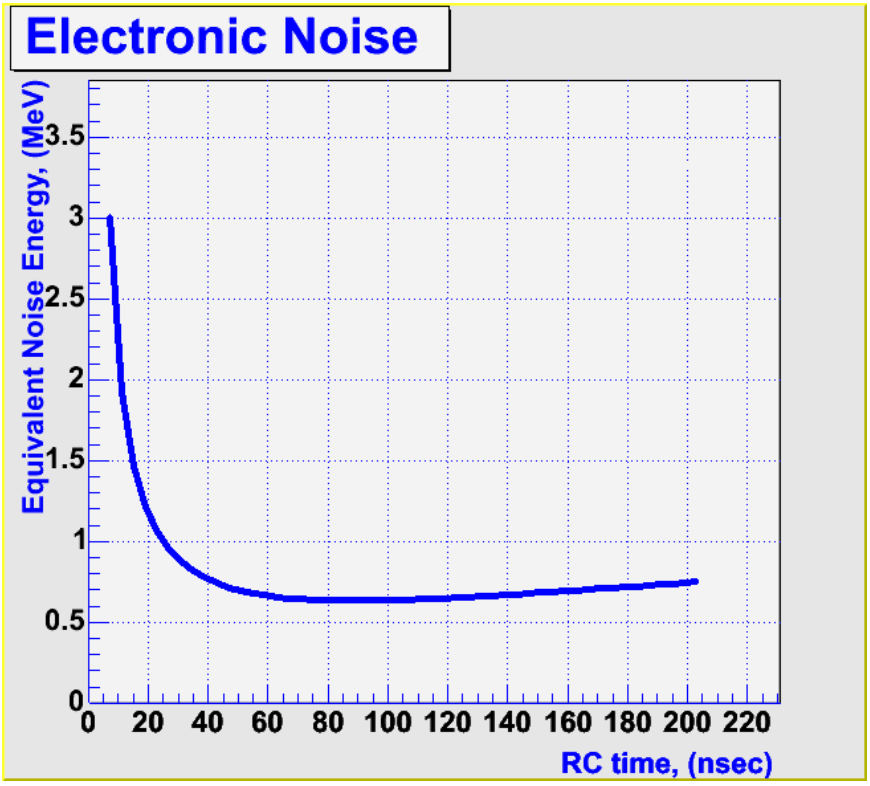

Figure 1-10: Equivalent electronic noise energy versus RC filter time.

The parameters given in the Table 1-3 are used in the calculation. The rise in the equivalent noise energy at small times is due to the series noise while parallel noise gives rise to the increase at large values of the shaping time.

The photostatistics error contribution includes the effect of the excess noise factor and the loss in signal for shaping times short compared to the time over which the light is collected. This last factor depends on the deviation of F(t_{max}) from its value when the APD current produced by the light source is an impulse.

The output voltage of the filter rises to a maximum $F(t_{max})Q/C_f$ at $t = t_{max}$, where Q/C_f is the output voltage of the preamplifier with feedback capacitance C_f . If the duration of the input current pulse from the diode is short compared to the *RC* time constant of the filter, $F(t_{max})$ is independent of the time constant.

In the NYU bench tests described in Section 1.11 below, the equivalent electronic noise energy (RMS) was measured to be 0.7 MeV for crystal with a summed 2 APD readout for the crystal size 3×3×14 cm^3 that was modeled here, and extrapolated to 1.1 MEV for the chosen 3.75×3.75×12 cm^3 crystal size of the calorimeter.

1.4.3 Light Collection

The equivalent noise energy is inversely proportional to the collected light L and the photostatistics error decreases according to $1/\sqrt{L}$. We can estimate the value of L given in the table Table 1.3 as follows. A Monte Carlo simulation was made of the light collection from a polished,

wrapped crystal 3×3×14 cm^3 with index of refraction 2.15, coupled at one end to a detector of refractive index 1.5. The light passing through the detector face originating from a source at the far end is 22.5% of the total. The mean distance traveled by the light is 20.4 cm, far less than the attenuation length above 400 nm of any of the crystals considered {Kampert:1994}.

We calculate the e-h pairs yield L of the wrapped $PbWO_4$ crystal (cooled) with size 3×3×14 cm^3 below:

L =	360	× 0.225	× 2.3	× 0.19	× 0.55	= 19
	LightYield (warm) (photons/MeV	MC light collection	Improvement from cooling	Area Frac.	QE	$\frac{e-h\ pairs}{MeV \cdot photodiode}$

where Area Frac is the fractional area covered by the photodiode (1.69 cm^2/ 9 cm^2 per APD) and QE = 55% is the nominal quantum efficiency for the RMD APD in the range of wavelength 430 nm. This estimate for the parameter L is in agreement with the measured value of 19 e-h pairs/MeV described in Section 1.11. However, such a perfect agreement should be considered fortuitous, since there are certainly 20% uncertainties in the experimental measurement.

The estimate is also consistent the 3 e-h pairs/(MeV-diode) obtained for $PbWO_4$ by the CMS Collaboration for crystal size 2.2×2.2×20 cm^3 at room temperature (20 °C). CMS used Hamamatsu APD with quantum efficiency 0.72 and an area of 0.5×0.5 cm^2 . Cooling to –24°C improves the light output by 2.3 {Lecoq:1995}.

1.4.4 Pileup

Pileup from background processes in which the rate is high but the energy deposition small can be treated, after suitable averaging, as an additional source of parallel noise. Single events in which a large amount of energy is deposited in a cell in coincidence with a DIO electron can produce an increase in the trigger rate. In coincidence with a conversion electron, such events result in a mismeasurement of the energy and lessen the detector's effectiveness as an extra, strong constraint on the event. This trigger rate increase is studied below and is expected to be low. The granularity of the detector is fine enough that such random high energy processes in coincidence with a conversion electron do not produce a substantial resolution tail.

The principal sources of energy deposition in the calorimeter are:

A. Beam electrons interacting in the either the muon target or, downstream in the muon beam stop.

B. Beam muons undergoing a large angle scatter in the target.

C. Neutrons originating from muon capture in the target or beam stop.

D. Photons from muon capture in the target or beam stop.

E. Photons radiated by decay electrons of energy E_e < 55 MeV originating from muons that stop in either the target or beam stop.

F. Electrons from muon decay in orbit, E_e > 55 MeV, in either the target or beam stop.

The cell pileup noise for these different processes is shown in Table 1.4

Pileup as Parallel Noise

Processes A – F were studied using GEANT. The pileup noise from each source is estimated by setting the signal contribution from the source equal to the RMS voltage produced by that source. Thus,

$$V_{rms}^2 = \sum_i n_i \cdot \left(\frac{\Delta Q_i}{C_f} \right)^2 \cdot \int_0^\infty \left| f(t) \right|^2 dt$$

where the RMS charge ΔQi is deposited at mean rate n_i from background source i, and

$$V_{rms} = V_{signal} = \frac{Q_{signal}}{C_f} \cdot F(t_{\max})$$

The equivalent noise energy due to pileup is then

$$ENE^2 = \tau_{pileup} \cdot \sum_i n_i \cdot \overline{\Delta E_i^2}$$

where $\overline{\Delta E_i^2}$ is the mean square energy deposition from background source i and

$$\tau_{pileup} = \frac{1}{\left| F(t_{\max}) \right|^2} \cdot \int_0^\infty \left| f(t) \right|^2 dt$$

The function $f(t)$ is the full electronic transfer function and includes the light source as a single exponential with the decay time 25 nsec. The value of τ_{pileup} for an *RC* time constant of 50 nsec is 143 nsec.

The pileup noise is estimated for each of the background sources using GEANT calculations of $\bar{n}$ and ‹$(\Delta E)^2$›. The results are collected in Table 1.4. The contributions from the muon target and the beam stop are given separately. The above method does not strictly apply to process A, since all of the particles are produced promptly as a flash during the micropulse; nevertheless, a reasonable estimate may be obtained, as discussed below. The other exceptional case is when the rate is low, even when summed over the nine cells assumed required to capture all the energy. A tail in the resolution at high energy results; this is discussed separately below.

A. Beam electrons

The yield of electrons produced in the tungsten target was found using GEANT and the hadron code GHEISHA. The number of electrons per primary proton that arrive at the muon target is approximately 0.16.

Figure 1-11 gives the arrival time distribution for these electrons at the exit of the transport solenoid. The electron time is smeared up to 100 ns due to the dispersion in the electron path length.

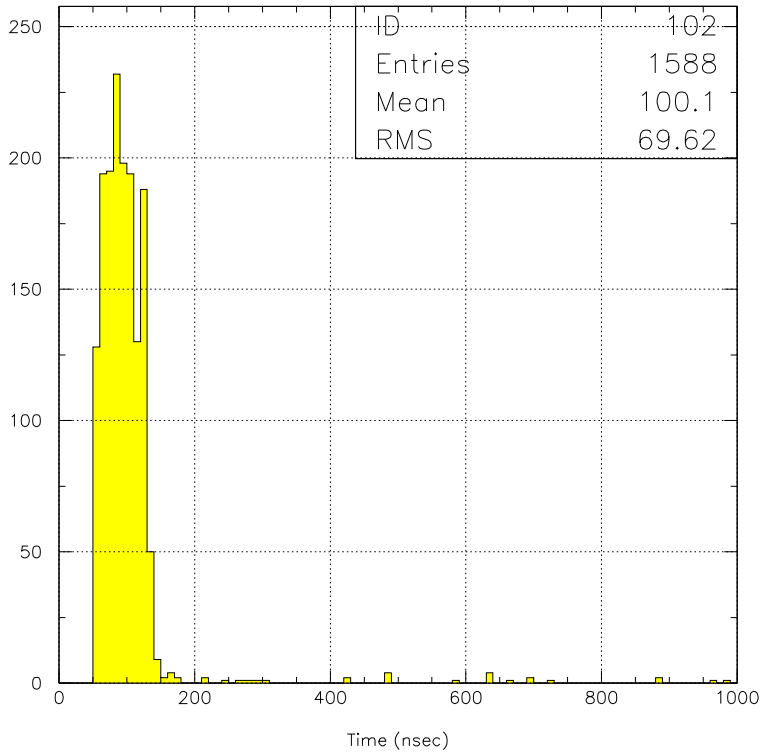

Figure 1-11: Distribution in time of arrival of the beam electrons at the exit of the transport solenoid. The proton beam strikes the target at t = 0.0.

Assuming a micropulse every 1.35 μs, the 4×10^{13} protons are shared among 3.7×10^{5} micropulses during the half-second spill. The electron intensity per micropulse at the muon target is

$4{\times}10^{13} \times (1/3.7 \times 10^{5}) \times 0.16 = 1.7 \times 10^{7}$

These electrons pass harmlessly down the center of the detector solenoid, except for those interacting in the muon target. Photons produced in the target can strike the front and inner surface of the calorimeter but not the main electron incidence face. The probability that this process results in an energy deposition above 10 keV in one of the 160 front and inner surface cells is 1.1×10^{-3}. The mean energy deposition is 2.9 MeV. The photons from this source would produce a substantial flash every micropulse in the bounding inner and front crystals:
$1.7 \times 10^{7} \cdot 1.1 \times 10^{-3} \cdot 1/160 \cdot 2.9$ MeV = 340 MeV/crystal

The flash occurs at least 600 ns before the gate is opened to detect the conversion electron. The light from the crystal is attenuated during this interval according to the decay time 25 nsec. These photons do not strike the ESS, but only the bounding crystals. This is evident in the GEANT simulation because the inner crystals do not see this energy deposition. The light left over from the flash is greatly attenuated in $PbWO_4$ because of the rapid exponential decay of the light and the ~500 ns that the crystals have to recover. For the $PbWO_4$ crystals the noise is negligible, even if the crystals are unshielded.

B. Beam muons

A beam muon with more than ≅50 MeV/c undergoing a large-angle elastic scatter in the muon target changes its trajectory sufficiently to stop in the low Z material of the proton absorber or the tracker. The muon then decays into an electron with energy up to 53 MeV with a decay time close the muon lifetime of 2.2 μs. For low Z materials the muon capture probability is negligible compared to the muon decay probability; this is a consequence of the Primakoff Z^4 law.

The probability that a muon undergoes a large angle scatter in the target and stops in the proton absorber {meco049} is 4.4×10^{-6}. The probability that the electron from the decay of a muon in the absorber strikes the calorimeter is 0.3. The total probability of this sequence is

$0.3 \cdot 4.4 \times 10^{-6} = 1.3 \times 10^{-6}$:

The number of muons incident on the Al target is 1.5×10^{11} Hz. The calorimeter hits occur mostly in the inner 128 (32×4) boundary cells. The energy deposition is 5.2 MeV/cell with 2.6 cells struck on average. The mean rate in each crystal is determined by multiplying the hit rate by the average cell multiplicity per hit. The pileup noise from this source is given in column two of Table 1.4.

$$\bar{n} = 1.5 \times 10^{11} \cdot 1.3 \times 10^{-6} \cdot 2.6 \cdot 1/128 = 3.9 \times 10^{3} \text{ Hz}$$

C. Neutrons from muon capture

Neutron background is considered as a source of pileup and as a source of radiation damage to the APD's. Neutrons above ~200 keV can damage the APD by displacing silicon atoms in the crystal {Hall:1990}. The damage can result in a substantial increase in the bulk leakage current and associated noise. This is discussed in Section 1.5.2.

The neutron spectrum is obtained from experimental data {Singer:1974},{Mukhopadhyay:1977}. Neutrons with kinetic energy below 10 MeV are produced with a spectrum characteristic of nuclear boil-off. There is an exponential tail above 10 MeV. The average number of neutrons emitted per muon capture increases with atomic number and is described well by the empirical function $(0.30 \pm 0.02)A^{1/3}$ {Singer:1974}. The measured average number of neutrons per capture on Al is 1.26 ± 0.06. In our calculations, the spectrum is normalized to 1.2 neutrons per stopped muon and is cut off at an upper energy of 50 MeV.

The neutron background from muon capture is simulated using the distribution of muon stops in the Al target. GEANT and the hadron code GCALOR are used to track the primary neutrons, generate subsequent interactions, and calculate the resultant neutron flux and energy deposition in the calorimeter.

The number of muons captured during the 0.5 s AGS spill is

$4 \times 10^{13} \cdot 2.5 \times 10^{-3} \cdot 0.6 = 6 \times 10^{10}$ /spill

where the first number is the proton intensity, the second is the number of stopped muons per proton, and the third is the probability of capture. Neutrons associated with capture may hit the calorimeter; each capture gives 1.2 neutrons and these in turn interact with material in the Detector Solenoid environment (in the detectors and supports, cryostat, cryostat walls, and return yoke and outside shielding) leading to more neutrons. Two 10 m long cylindrical polyethylene (CH_2) shields are used to

reduce the neutron flux at the calorimeter. In this simulation, one shield of thickness 20 cm is located outside the cryostat just inside the steel return yoke (35 cm thick Fe), which serves also as part of the cosmic ray shield. A second polyethylene shield of thickness 10 cm is located just inside the cryostat wall (7 cm thick Al). Figure 1-12 shows the neutron energy spectra with the polyethylene shielding. The integrated flux is reduced ten-fold by the presence of the polyethylene.

The neutron energy threshold to displace silicon atoms in the APD is 0.2 MeV. The probability that a neutron with energy more than this threshold crosses the back surface of the calorimeter is 1.7×10^{-4}. When integrated over the duration of the experiment (107 sec) the flux through the APD's mounted on the back surface is

$6 \text{ x } 10^{10} \cdot \ 1.2 \cdot 1.7 \text{ x } 10^{-4} \cdot 10^{7} \cdot 1/3600 = 3.4 \text{ x } 10^{10} \text{ n/cm}^2$.

A similar calculation starting from muon stops in the beam shield adds 2.3×10^{10} *n*/cm^2. The sum, 6×10^{10} *n*/cm^2, will be used in Section 1.5.2 to estimate the radiation-induced bulk leakage current.

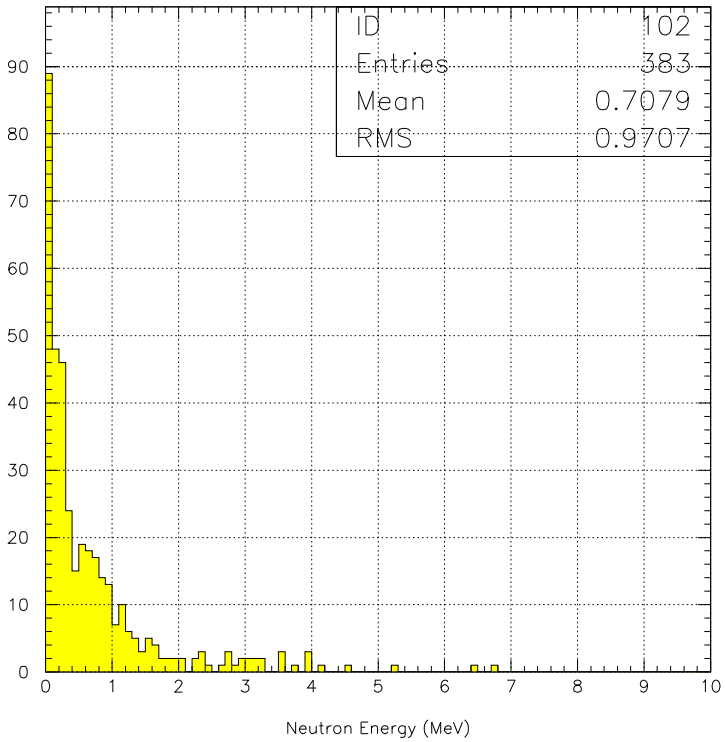

Figure 1-12: Neutron energy with the two of shields (10 and 20 cm thick CH2). Bin size is 0.1 MeV.

The probability that a primary neutron from the target leads to more than 10 keV energy deposited in the calorimeter is 1.8×10^{-3}. The hits are distributed over the 1000 cells of the calorimeter. The 6×10^{10} captures during the half-second spill is spread over 3.7×10^{5} micropulses, one every 1.35 μs. Approximately 54% of the captures occur during the 650 ns window extending from 700 ns to 1350 ns after the pulse. The number of neutrons/cell that deposit more than 10 keV during each gate window is

$(6 \text{ x } 10^{10} / 3.7 \text{ x } 10^{5}) \cdot \ 1.2 \cdot 1.8 \text{ x } 10^{3} \cdot 0.54 \cdot 1/1000 = 0.2/\text{cell}$.

Twenty percent of the gates will have a neutron. The RMS energy deposited is 1.3 MeV. The crystal hit rate $\bar{n}$ used in the pileup calculation is scaled by the average multiplicity of 1.8,

$(0.2 / 650 \times 10^{-9}) \cdot 1.8 \cdot 1.4 = 7.5 \times 10^{5}$ Hz ,

where the rate at the start of the gate, which is 40% higher, is used. A similar calculation is done for neutrons from the beam dump. The cell noise estimated in this way from the two sources is given in column three of Table 1.4.

D. Photons from muon capture

The photon spectrum is difficult to estimate. Every μ-capture results in the production of excited nuclear states. Assuming a at energy spectrum from 0 – 7 MeV, normalized to 1.8 photons per capture, the probability that photons above 10 keV strike the calorimeter is 2.3×10^{-3}, typically turning on 1.6 cells. The number/cell during each gate window is

$(6 \times 10^{10} / 3.7 \times 10^{5}) \cdot 1.8 \cdot 2.3 \times 10^{-3} \cdot 0.54 \cdot 1.6/1000 = 0.6$ /cell .

The RMS energy ΔE deposited is 1.8 MeV and $\bar{n}$ is

$(0.6 / 650 \times 10^{-9}) \cdot 1.4 = 1.2 \times 10^{6}$ Hz .

The noise from this source and from the beam dump are given in column four of Table 1.4.

E. Muon decay in orbit with E < 55 MeV

Forty per cent of the muons that stop in the Al target decay in orbit, producing an electron. Those of energy less than 55 MeV are confined to the central region of the solenoid by the strong magnetic field and do not hit the calorimeter. However, these electrons can radiate in the target. Photons from the electromagnetic shower deposit more than 10 keV in the front and inner 160 cells with probability 5.6×10^{-4}. The number of muons that decay during the half-second AGS spill is

$4 \times 10^{13} \cdot 2.5 \times 10^{-3} \cdot 0.4 = 4 \times 10^{10}$:

and the number of photons per cell during the gate window is

$(4.0 \times 10^{10} / 3.7 \times 10^{5}) \cdot 5.6 \times 10^{-4} \cdot 0.54 \cdot 1.6 / 160 = 0.33$,

where the 1.6 hit multiplicity was taken into account. The RMS energy deposited is 1.3 MeV and the crystal hit rate $\bar{n}$ is

$(0.33 / 650 \times 10^{-9}) \cdot 1.4 = 7.1 \times 10^{5}$ Hz .

The cell noise is calculated for this process in column five of Table 1.4.

F. Muon decay in orbit with E > 55 MeV

The probability that an electron with energy more than 55 MeV hits the calorimeter and releases more than 10 keV equals 2.8×10^{-5}. The calorimeter hits occur mostly in 80 (20 x 4) boundary crystal cells with an average energy release $\bar{E}$ = 3.9 MeV. The hits/crystal during the gate is equal to

$(4.0 \times 10^{10} / 3.7 \times 10^{5}) \cdot 2.8 \times 10^{-5} \cdot 0.54 \cdot 4.1 / 80 = 0.08$ / cell.

The hit rate is 1.8×10^{5} Hz; see column six of Table 1.4

Table 1.4: Pileup noise in crystal cells from different sources. Upper and lower number are for events originating in the aluminum target and muon beam stop, respectively. Flash from beam electrons (column 1) is attenuated using time constant of component of crystal light output that produced largest signal during gate. The noise is calculated from $\sqrt{\bar{n}\langle E^2\rangle\tau_{\text{pileup}}}$, where the mean rate and square of the energy are obtained from GEANT, and the time constant depends on the signal input shape and transfer function.

Background Source	**Beam *e***	**Beam μ**	**Neutron**	**Photon**	**DIO < 55 MeV**	**DIO > 55 MeV**
Rate, Hz	1.3×10^{13} 1.3×10^{13}	1.5×10^{11}	2.3×10^{11} 3.0×10^{10}	3.4×10^{11} 5.6×10^{10}	1.3×10^{11} 2.7×10^{11}	7.2×10^{8} 1.6×10^{9}
Hit Prob.	6.0×10^{-4} 4.0×10^{-3}	1.3×10^{-6}	1.8×10^{-3} 6.0×10^{-3}	2.3×10^{-3} 1.0×10^{-2}	5.6×10^{-4} 1.0×10^{-2}	5.1×10^{-3} 1.5×10^{-2}
Hit Cells	1000 1000	128	1000 1000	1000 1000	160 1000	80 1000
Cell $\bar{E}/\langle E^2\rangle$, MeV^{-1}	0.1/0.07 0.2/.25	5.2/90.5	0.7/1.6 0.9/1.7	0.8/1.8 0.9/2.0	0.6/1.2 0.4/0.8	3.9/75.0 0.6/1.3
Cell Mult.	1.2 1.3	2.6	1.8 1.9	1.6 1.7	1.6 1.5	4.1 2.1
Cell Rate, Hz	4.7×10^{6} 3.4×10^{7}	3.9×10^{3}	7.5×10^{5} 3.4×10^{5}	1.2×10^{6} 9.6×10^{5}	7.2×10^{5} 4.0×10^{6}	1.8×10^{5} 2.5×10^{4}
$PbWO_4$ Cell Noise RC=50 ns, MeV	0.0 0.0	0.22	0.4 0.3	0.55 0.52	0.35 0.67	1.4 0.1

The table is for the chosen crystal size of 3.75×3.75×12 cm^3. The total pileup noise from each source is added in quadrature, except for that in the last column, since DIO events above 55 MeV are reconstructed successfully as showers. The result is an RMS of 1.2MeV in the cell. For the original crystal size of 3×3×14 cm^3, the number was 0.9 MeV.

1.4.5 Pileup As Accidental Energy Deposition – Cell Occupancy

In the previous section the pileup was treated as a source of parallel noise; this works well for processes in which the rate is high compared to the inverse of the shaping time. In that calculation, the signals are integrated electronically producing a mean level (pedestal shift). The RMS fluctuations about

that level result in a Gaussian-shaped resolution broadening to the measurement of a signal in that cell. The same processes, pileup and electronics noise, are considered here to compute the rate of non-signal cells passing a threshold cut when energy deposition becomes significant compared to the resolution. The result is a high energy tail in the resolution function.

Table 1.5 gives the instantaneous rates in a vane as a function of the threshold energy. A shower typically occupies less than 2% of a vane, see Figure 1-8. The last row in Table 1.5 is the probability that there is accidental energy deposition in a shower above the threshold indicated and in the same 650 ns gate. The calculation of the previous section includes these contributions and is not independent. If the signal rises to its peak in, characteristically, 100 ns, as in the faster crystals, there is a 12% chance that 1 MeV is deposited in the tower and a 1.4% chance that five or more MeV is present. This probability becomes worse for longer integration times. Note that not all of the items in this table are of consequence. Beam electrons, for example, produce a flash that is gone by the time the gate in which the signal is detected is opened. Electrons from muon decay in orbit produce energy in a small fraction, 80/2000 ~ 0.04, of the cells.

Table 1.5: Instantaneous rate (MHz) for energy deposited in calorimeter vane to be above threshold. The probability that this energy is in the same tower and coincident within τ of a signal event is given by multiplying by $\approx \tau/50$. Light from beam electrons during ash is strongly attenuated before gate begins. DIO events affect only 240 cells. Last row is the summed probability there is an event in the full 650 nsec gate (see text).

Background Source	> 1 MeV	> 5 MeV	> 10 MeV
DIO > 55 MeV	0.74	0.41	0.29
Beam e's	23		
Beam μ's	0.04	0.032	0.027
Neutrons	25.0	1.4	0.45
Gammas	36.0	6.0	0.08
Probability, %	80.0	9.0	0.7

1.4.6 Combined Energy Resolution

The results of the resolution calculations are summarized for two crystal sizes in Table 1.6, and for the chosen crystal size Figure 1-13. With an *RC* time constant of 50 nsec, the signal reaches a maximum at t_{max} = 117 nsec. The cooling to – 20° C increases the light from the $PbWO_4$ crystal by a factor of 2.3 and decreases the bulk leakage current substantially. The current arises from thermally generated carriers and is strongly temperature dependent: $I_b \propto (kT)^{3/2} e^{-(1.2/2kT)}$ where kT is expressed in electron volts.

Table 1.6 presents the calculated results for photo-statistics noise σ_{PS}, electronic noise σ_{el}, pileup noise σ_{pileup}, pileup integral in τ_{pileup}, a time t_{max} when the signal reaches maximum. The total resolution for 100 MeV electron is obtained by summing in quadrature the electronic and pileup noise from 6 cells, after the software reconstruction of the calorimeter energy from the hit pattern. The contribution from shower fluctuations is obtained from a fit to the high energy side of the distribution, (see Figure 1-7) ignoring the low energy tail. A parameter of light collection yield L for two APD photodiode readout is taken from laboratory test measurements is equal 38 e-h pairs per MeV for the crystal size of $3 \times 3 \times 14$ cm^3. The extrapolated results for the bigger size of crystal $3.75 \times 3.75 \times 12$

cm^3 are based on the estimate of L equal to 24 e-h pairs per MeV for two APD readout. The combined resolution is 4.1 MeV for the smaller crystal of the study and extrapolates to 5.3 MeV for the chosen crystal size.

Table 1.6: Resolution obtained for a $PbWO_4$ crystal with 2 avalanche photodiode readout. The top line is the result of these studies for the smaller crystal. The bottom line gives the extrapolation to the chosen Crystal size.

Crystal, p.e./MeV	# APD's	RC, ns	σ_{PS}, MeV	σ_{el}, MeV	σ_{pileup}, MeV	σ_{tot}, MeV	Pileup τ_{pileup}, ns	t_{max}, ns
$PBWO_4$ (-20 ºC) [3×3×14] L = 38	2	50	2.4	1.7	2.2	4.1	143	117
PBWO4 (-20 ºC) [3.75×3.75×12] L = 24	2	50	3.0	2.7	2.9	5.3	143	117

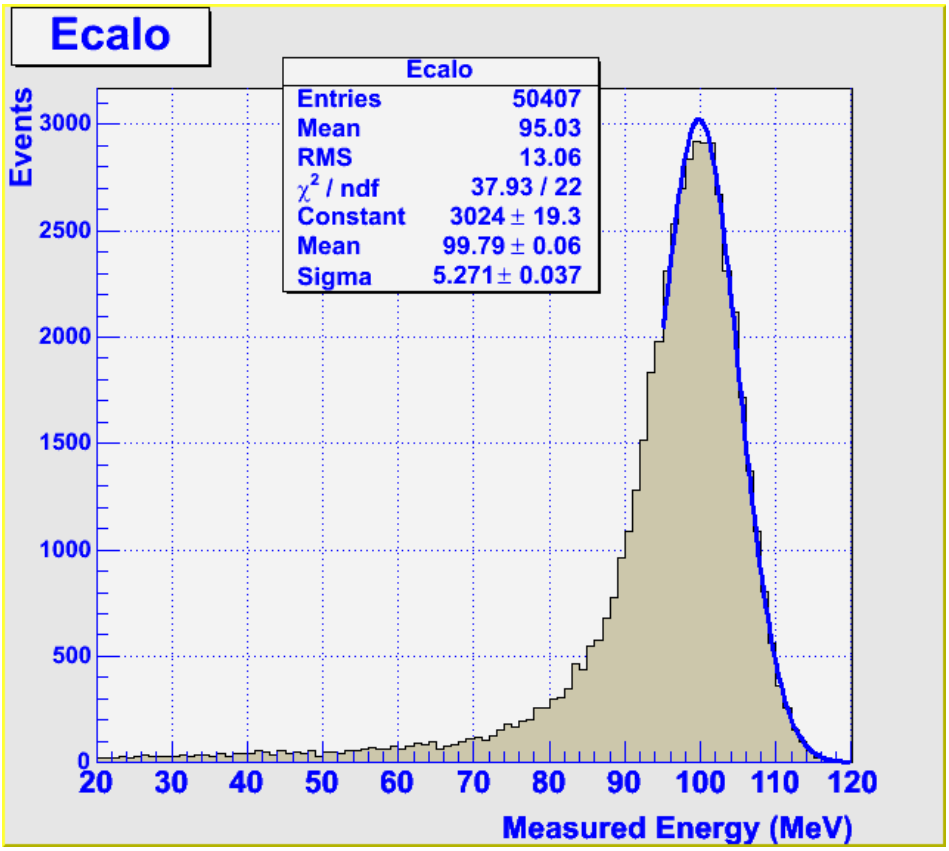

Figure 1-13: Folded total resolution for the chosen crystal size of 3.75 cm x 3.75 cm. Plotted is the predicted distribution for the measured electron energy. Shower fluctuations (GEANT), photo-statistics, pileup, and electronic noise are included.

1.5 Radiation Induced Effects

The impact of radiation exposure on both the crystal and the diode must be considered.

1.5.1 Radiation Damage in the PbWO4 Crystals

The effect in lead tungstate may be summarized as follows {Annekov:1997}, {Chen:1998}, {Annekov:1999}:

- The blue and green radiating centers are not damaged by irradiation; the scintillation mechanism in the region of wavelengths of interest is unaffected.

- Radiation damage in the crystal is caused by the conversion of existing defects in the crystal lattice to light absorbing color centers, resulting in a radiation-induced absorption length. For one defect type, during a time interval dt:

$$dN_c = (N_d - N_c)\frac{S}{d}dt - N_c\omega dt \ , \qquad N_c = N_d \frac{S/d}{\omega + S/d}(1 - e^{-(\omega + S/d)t}) \ ,$$

  where S is the dose rate, ω the recovery rate, and d the damage constant. The induced absorption is $k_{\text{induced}} \equiv 1/\lambda_{\text{induced}} = \sigma N_c$, where σ is the absorption cross section for light at a color center. The damage saturates for long exposures at a level that depends on the dose rate:

- The radiation damage from photon irradiation is reversible. Heating for a few hours to 200°C restores the initial light yield.

- The induced absorption at an accumulated dose of 500 Gy from ^{60}Co irradiation is not more than 0.8 m^{-1}.

The last item is the specification from the crystal manufacturer for the crystals purchased . The induced absorption cannot exceed σN_d, where N_d is the number of defects (typically a few ppm of the crystal sites).

The results of calorimeter irradiation simulations, using GEANT are shown in Table 1.7. The mean energy deposition per event (typically a muon that is captured or decays in the aluminum target or the material of the beam dump) is given in the first row of the table, and the total energy deposition during the experiment (10^7 s) appears in the second row. The calorimeter mass affected is given in the third row. Neutrons interact uniformly throughout the entire calorimeter, 1226 kg, while some of the soft gammas and electrons from muon decay in orbit affect only the crystals on the perimeter of the detector. In calculating the radiation dose,

$$\frac{1}{\rho}\frac{dW}{dV}$$

in J/kg (Grey), note that the gammas are assumed to be absorbed in one radiation length, 0.89 cm in lead tungstate. At an energy of 0.1 MeV, typical of photons produced promptly during the beam flash (column 2), the attenuation length in the crystal is due mostly to the photoelectric effect, and is ≈0.02 cm, 45 times smaller. This leads to very high dosage in a thin surface layer of crystal. The rate is reduced dramatically and the measurement is unaffected by a thin high *Z* cover (~ 2mm of Cu) over the electron sensitive surface. Only these photons from the flash, originating in the beam dump, produce a radiation level of any consequence.

Table 1.7: Irradiation of $PbWO_4$ calorimeter from different sources. Levels from interactions in the Al target (AT) and muon beam stop (MBS) are given separately. The energy deposition of electrons and photons is assumed to take place in one radiation length {meco052}.

ΔE AT MBS, Units	0.1 0.2	0.7 0.9	0.5 0.8	0.5 0.2	14.2 0.6
Energy Dep. AT MBS, Joules/Expt	1250 16600	464 260	625 720	58 860	83 4.3
Affected Mass AT MBS, Kg	133 133	1788 1788	133 133	133 133	5.5 133
Dose Rate AT MBS, 10^{-2} Gy/hr	0.4 5	0.01 0.007	0.2 0.2	0.02 0.23	0.6 0.001
Dose/Expt AT MBS, Gy	10 125	0.3 0.2	4.7 5.4	0.5 6.5	15 0.03

1.5.2 Radiation-Induced Dark Current in the APD

We estimate the increase in the dark current in the APD caused by neutrons from the sources discussed in Section 1.4.4. The effect of the radiation is to displace atoms from sites in the crystalline lattice {Hall:1990}. The radiation induced leakage current, I_B^{irr}, depends on the number of displaced atoms. It is proportional to the relevant detector volume and increases linearly with exposure time. The proportionality constant α is strongly temperature dependent.

The current depends sensitively on the temperature {Baccaro}{Borchi:1994}{Moll:1999} and can be reduced substantially by cooling:

$$I_B^{irr} \propto T^2 \exp(-\varepsilon_T / 2kT) \quad ,$$

where ε_T = 1.2 eV. The decrease is significant even for small temperature changes, -9%/ °C at T = 20 °C. For a temperature change from +20 °C to −20 °C, I_B^{irr} decreases by a factor 50.

The radiation-Induced bulk current at room temperature is {meco062} :

I_B^{irr} = 8×10^{-17} A/(n · cm) x 5×10^{-4} cm x 1.7 cm^2 x 6.0×10^{10} n/cm^2 = 4 nA

A at 18 ºC | depletion depth x area | n flux/exp

or I_B^{irr} = 0.08 nA at temperature -20 C. The value of I_B^{irr} should be compared to the 0.05 nA used in the noise estimates.

The radiation induced dark current I_D^{irr} decreases with time. Experiments indicate several components with different lifetimes {Bosetti:1994}{Baccaro}are present:

$$I_D^{irr} = I_D^{irr}(0)\sum_i g_i e^{-t/\tau_i}$$

with g_i and τ_i given in Table 1.8.

Table 1.8: Dark current coefficients and decay times at 18 °C in lead tungstate, $PbWO_4$, crystals.

Coefficient	g_i	τ_i
1	0.20	12.9 min
2	0.30	85.4 min
3	0.13	30.5 hr
4	0.13	6.6 days
5	0.24	∞

We conclude that radiation damage effects do not lead to a significant degradation of the resolution of the calorimeter during the 10^7 second lifetime of the experiment.

1.6 The Nuclear Counter Effect in the APD

The APD nuclear counting effect can produce a large APD (minimum ionizing muon equivalent) signal in Si, an average energy loss 1.664 MeV/g cm^2 · 2.33 g cm^{-3} = 3.88 MeV/cm. To produce an electron/hole pair an energy 3.62 eV is required. We thus expect to collect 107 e-h pairs/µm for a minimum ionizing track. The main junction of the “gain region”, where the avalanche gain takes place, is located at ~50 µm inside the APD. So the estimated number of e-h pairs from the APD nuclear counting effect is ~5000. This number is comparable to the number of e-h pairs from a 100 MeV electron signal in a PbWO4 crystal: 30 e-h/MeV/APD ·100 = 3000. The APD "drift region" without gain is ~ 200 µm. Because of the high APD gain the contribution to signal from the "drift region" is negligible.

To study the energy resolution {meco103}, radial and longitudinal leakages versus crystal length of a simple setup of PbWO4 cylinders of fixed radius R = 13 X_0 = 11.57 cm and variable length L = 12 - 18 X_0 were selected. The radiation length X_0 for the PbWO4 crystal is 0.89 cm.

The probability of photon, electron and positron leakage is defined as: The number of photons, electrons and positrons crossing the PWO4 (front, radial and back) crystal surface normalized by primary 100 MeV electrons incoming along the PbWO4 cylinder axis, multiplied by 100%. Figure 1-14 shows the probability of photon leakage through the PbWO4 back surface versus PbWO4 length as determined with a GEANT 3 shower simulation.

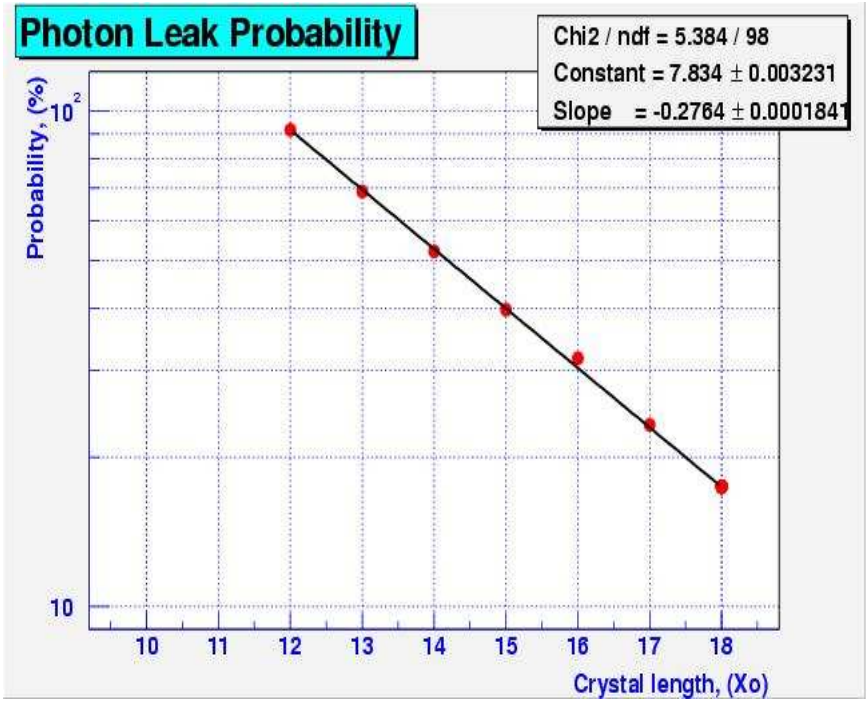

Figure 1-14: The probability of photon leakage through the crystal back surface versus PbWO4 crystal length.

The probability that a cascade photon crosses the APD "gain region" and produces a high pulse signal is 2.4×10^{-3} .

Figure 1-15 shows a probability of electron leak through the PbWO4 back surface versus PbWO4 length.

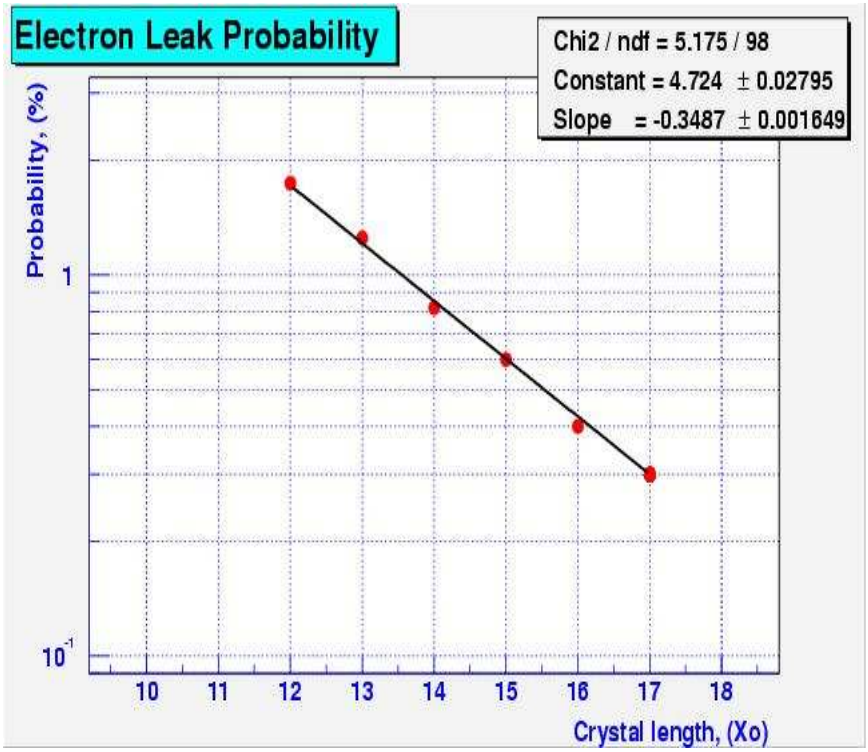

Figure 1-15: The probability of electron leakage through the crystal back surface versus PbWO4 crystal length.

The probability that a cascade electron or positron crosses the APD "gain region" and produces a high pulse signal is 9×10^{-4} and 4×10^{-4} respectively.

We thus find that the total probability that an electron, positron and photon produced in the cascade of a 100 MeV electron interact in the gain region ~50 μm of the APD is small, ~ 3.7×10^{-3}. The number of e-h pairs produced in such events, > 2500, are equivalent to the signal from a 100 MeV conversion electron.

1.7 Readout, Trigger Rates

The beam structure imposes severe constraints on the readout if there is a flash produced when the protons strike the production target. Beam electrons, for example, produce such a flash in the bordering cells of the calorimeter if they are unshielded. For this source, it appears that some of the flash can be eliminated by shielding. The readout scheme described below assumes that such a flash does occur, and that all of the analog signals have to be held before the next beam micropulse. Two possible timing schemes have been considered. For most of our studies, the structure assumed consisted of one pulse of 100 ns duration every 1.35 microseconds filled by one booster cycle to an intensity $\leq 2 \times 10^{13}$ protons. This is accomplished by filling two of six equally spaced buckets around the ring. The gate for detecting the conversion electron extends from 600 ns to 1250 ns, 100 ns before the next beam pulse. A conversion electron coming near the end of the gate has to be held before the next pulse. One hundred nanoseconds should be sufficient for $PbWO_4$. The time required for a calorimeter signal to get to its maximum is approximately 120 nsec for the shaper RC equal 50 nsec.

An alternate mode of operation might be to fill and extract the beam in one micropulse every 2.7 microseconds. The pulse would be filled by the two booster cycles to an intensity of $\leq 4 \times 10^{13}$ protons.

In this mode, the gate extends from 0.8 μs to 2.3-2.6 μs, depending on the shaping time. The gate acceptance is larger by 20 – 30%, but there is a loss of a factor of 2 in the number of filled buckets. It is not clear how much the maximum beam in a bucket could be increased in this mode. This option is being studied in the context of the beam extinction.

The level 1 trigger is formed by dividing each bar of the calorimeter into 48 overlapping supercells. Each supercell is obtained by summing signals, after filtering, from a 4×4 arrays of crystals. There are two possible implementations of the trigger. This summing is done either in analogue-summed trigger towers, or by fast processing of continuously sampled digitized signals for a digital trigger. In this version, the sums from the 48 supper-cells are encoded with FADC's every ~25 ns and fed to a pipeline processor. This readout scheme is similar to many used in previous experiments and we hope to borrow from this experience.

When the energy in any super-cell is greater than a preset threshold, the sampling clock is stopped and the analogue data is digitized and read out for the tracker as well as the calorimeter. The trigger is then further refined by software to produce a reduced event rate higher level trigger to be written into a storage device (See the Chapter on the DAQ system).

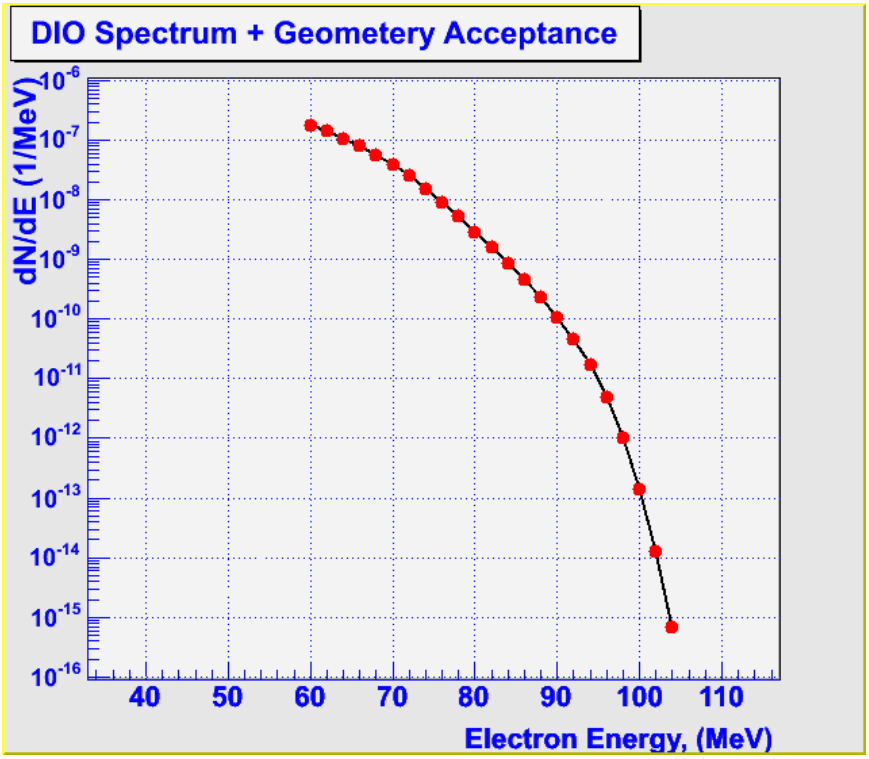

Figure 1-16: A Differential energy spectrum for muon decay in orbit in Al multiplied by calorimeter acceptance.

The events that trigger the detector come principally from muon decay in orbit with an energy deposition peaking near the threshold energy of ~80 MeV A GEANT simulation including the calorimeter acceptance determines the energy deposited in each cell of the detector, which is then smeared by electronic, photostatistics, and pileup noise, to produce the spectrum of Figure 1-16, which is then used to calculate the trigger rate.

In Table 1.9, the trigger rate and detector efficiency are given for two energy thresholds for the super-cells, with all resolution effects included. Because there are 16 cells summed in a super-cell the

resolution is worse than for the ~6-cells summed for the reconstructed energy of Section 1.4.6. The total energy resolution for super-cells (16 crystals), including shower, photostatistics fluctuations and electronic and pileup noises, is found to be 5.4 and 7.9 MeV for crystal size 3×3×14 cm^3 and 3.75×3.75×12 cm^3 respectively. It is the latter that corresponds to our chosen crystal size. An efficient trigger at an entirely manageable rate of order 1 KHz is achievable.

Table 1.9: Trigger rate and efficiency vs. threshold energy in supercell 4 × 4 arrays of crystals. The energy in cells is generated by GEANT and smeared by electronic noise, photostatistical fluctuations, and pileup noise.

$E_{threshold}$, MeV	Triger Rate, kHz σ = 5.4 MeV crystal 3×3×14 cm^3	Triger Rate, kHz σ = 7.9 MeV 3.7×3.7×14 cm^3
75	0.8	1.4
80	0.3	0.5

1.8 Lead Tungstate Crystal Measurements

Lead tungstate provides the high density and fast signal required in this application and at low cost, but the light output is small and considerable care will be required to keep electronic noise from dominating the resolution. Substantial progress in the development of these crystals has been made in the last few years. To begin the process of crystal selection, discussions with the manufacturers of this crystal were initiated and ten 3 cm × 3 cm × 14 cm crystals were purchased from the Bogoroditsk Technochemical Plant in Russia. Measurements of the properties of the ten crystals received were made at BNL by C. Woody and S. Stoll. The transmissivity of the crystal along its long axis was measured using a variable light source as illustrated in Figure 1-17.

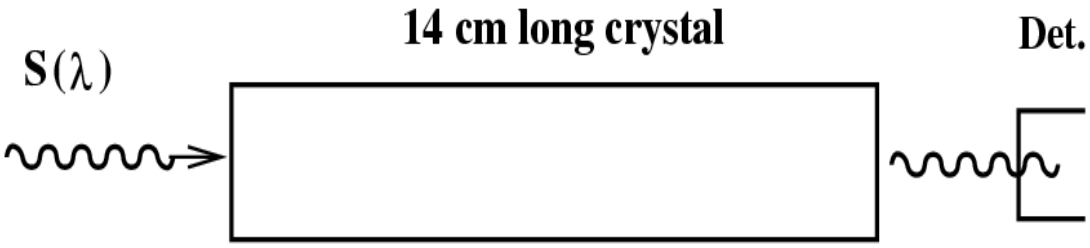

Figure 1-17: Measurement of transmission as a function of wavelength; results in **Figure 1-18**

The results of measurements on five of the ten crystals are superimposed in the plot of Figure 1-18. The remaining five crystals give identical plots. Reflection off the first surface and repeated reflections off the second limit the transmission at long wavelength to

$T = (1-R)/(1+R) = 0.763$, and $R = (n-1)^2/(n+1)^2 = 0.135$

where the index of refraction n = 2.16 at 632 nm is used .

As is shown in Figure 1-18, the measured value at this wavelength is 0.753, which corresponds to an index 2.20 if there is no absorption. In the visible region 400 – 700 nm, the dispersion is normal; the index of refraction increases with decreasing wavelength, reducing the transmission through the crystal even if the absorption is small. In optical glasses, the index increases by approximately 1% between 400 – 700 nm. Ignoring this effect, and attributing the measured 5.4% decrease in transmission

from 630 nm to 400 nm entirely to absorption in the crystal, a lower limit of 2.6 m is obtained for the absorption length at 400 nm. This distance is 19 times greater than the crystal length. At an exposure of 500 Grays, considerably greater than the level expected in the experiment (see below), the absorption length should still be greater than 1.2 m, 8-10 times the crystal length.

The slope of the rise in the approximately linear region between 340 nm and 370 nm has been correlated with the radiation hardness of the crystal {Auffray}. For the longer CMS crystals, those with slopes of greater than 1.5%/nm, the light loss is less than 6% after exposure to low level radiation (1.5 Grays total at 0.15 Grays per hr), while for crystals with smaller slopes the degradation in light output is typically 4 – 5 times larger. The steep slope of the rise in Figure 1-18 2.6%/nm, is a good sign in this regard.

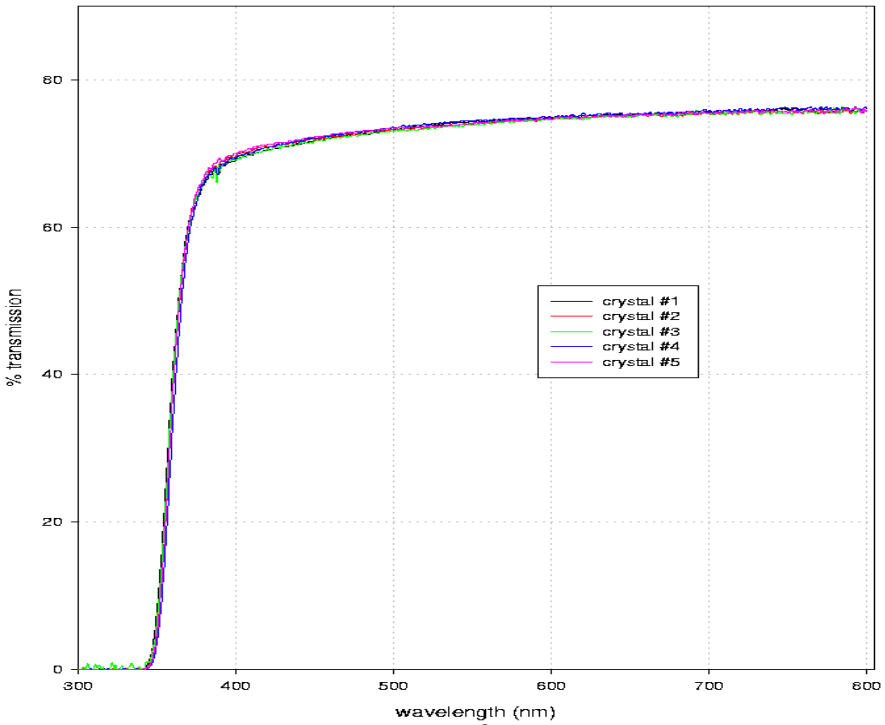

Figure 1-18: $PbWO_4$ crystals, $3 \times 3 \times 14$ cm^3. Measured transmission, 5 crystals obtained from Bogoroditsk Technochemical Plant, Russia.

In Figure 1-19 the light output, in photoelectrons/MeV, is measured as a function of position along the crystal with a ^{137}Cs source. A pre-calibrated Hamamatsu R2059 photomultiplier tube that covers the end of the crystal is used in the measurement. The source is moved along the 14 cm long crystal and measurements are made at 2, 4, 7, 10, and 12 cm. The uniformity, (max - min)/min, averages 3.4% for ten crystals and varies from 1.8% (best) to 4.8% (worst). The light yield is approximately 15 photoelectrons/MeV. The plot also shows the superiority of Tyvek to Teflon wrapping for collecting the light.

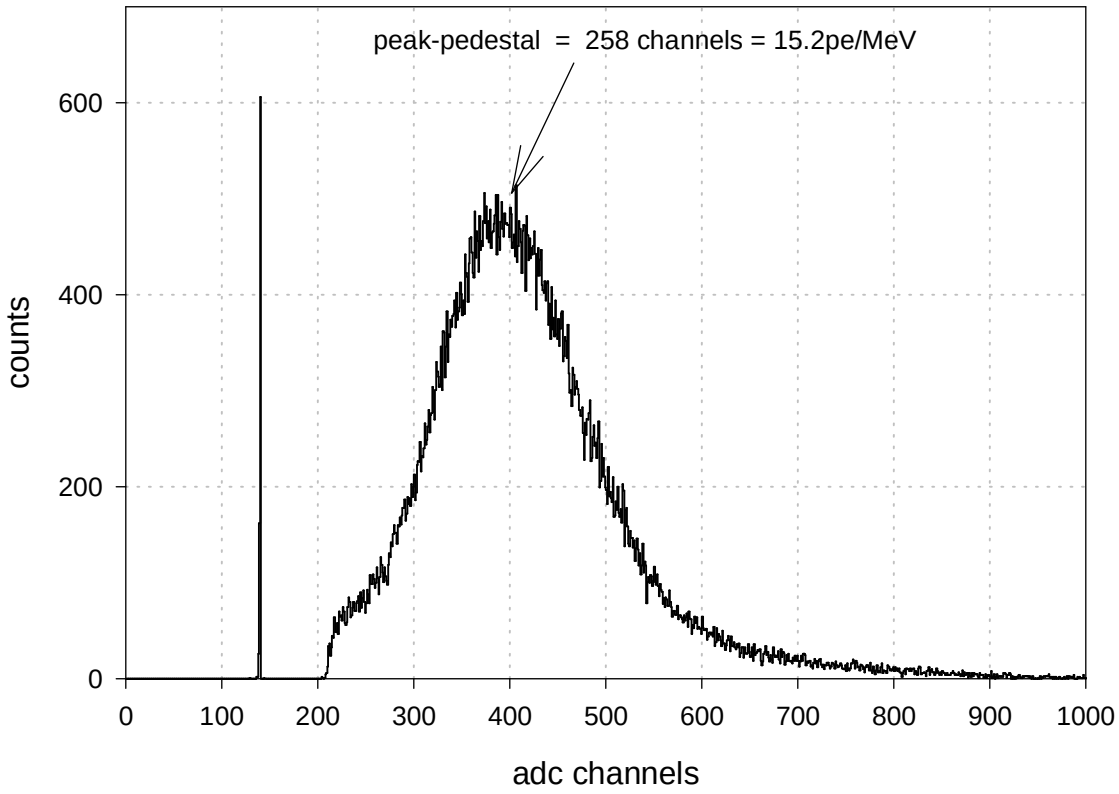

Figure 1-20: Measured light output spectrum using a ^{137}Cs source at far end of $PbWO_4$ crystal. The signal represents fifteen photoelectrons/MeV into Hamamatsu 2 in R2059 photomultiplier tube.

1.9 Avalanche Photodiode Studies

Their ability to operate in a high magnetic field, their high quantum efficiency (around 50%) and their compactness make avalanche photodiodes (APD's) the natural light detector for the crystal calorimeter. A likely candidate for the APD's for reading out the scintillation light of the PWO crystal is the Radiation Monitoring Devices (RMD) Model S1315 large area APD with a square active area of 13 mm X 13 mm. Properties of one such APD were measured with a blue LED at NYU {meco126}.

The Gain of the APD (output electrons/input photoelectrons) vs. the APD's reverse bias voltage is shown in Figure 1-21, for two temperatures. A typical stable operating point is a gain of 300, with a HV of about 1500V. For a given HV, the -24^0 C gain is higher by a factor of about 4 than the gain at room temperature. For a fixed gain of 300, the needed bias voltage is about 100V less at -24^0 C than at room temperature.

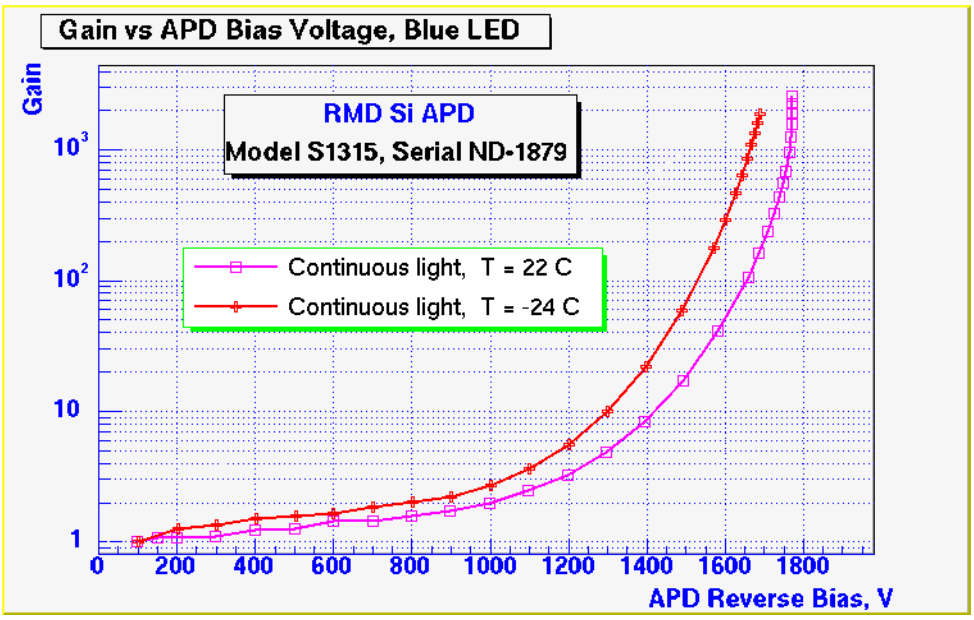

Figure 1-21 APD Gain versus Bias Voltage at two temperatures.

The biggest advantage of operating the APD at low temperature is shown in Figure 1-22, which displays the ratio of Dark Current to Gain versus the Gain. This ratio is a good figure of merit, since it measures the dark current in units proportional to the signal output of the APD. At a gain of 300, the dark current, dominated by the APD bulk current, drops by a factor of 200 at -24^0 C, compared that at room temperature, leading to a significant improvement in the electronic noise.

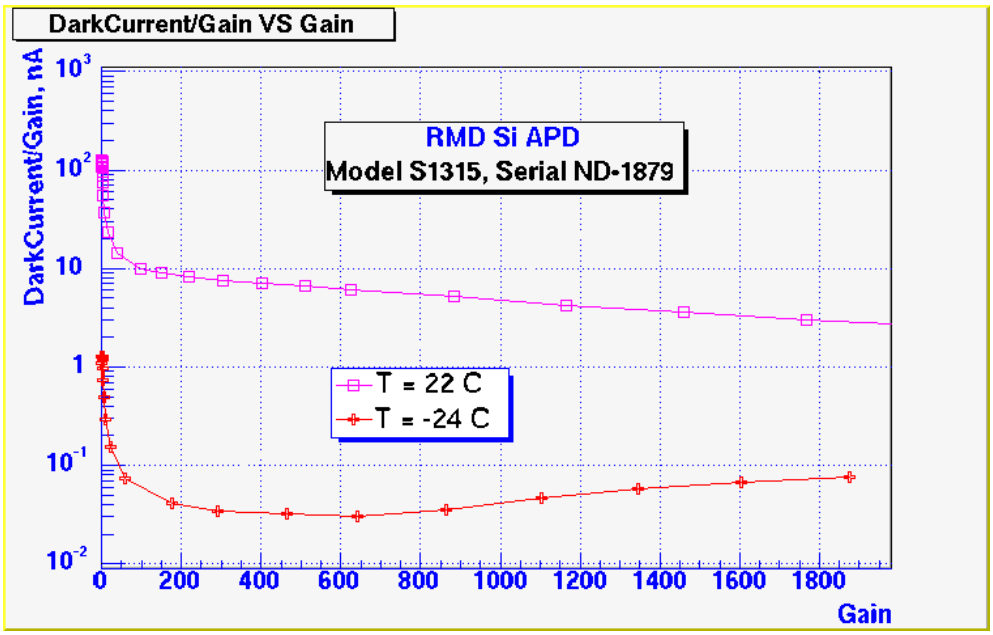

Figure 1-22 The ratio of dark Current over gain vs. gain.

In Figure 1-23 the derivative of the fractional gain with respect to bias voltage is plotted versus Gain (M). It is seen to increase rapidly at room temperature, but stay nearly constant at about 2% / Volt at -24^0 C. This sets the scale for the requirements on the high voltage supply, control of the bias HV to better than 1/2 volt.

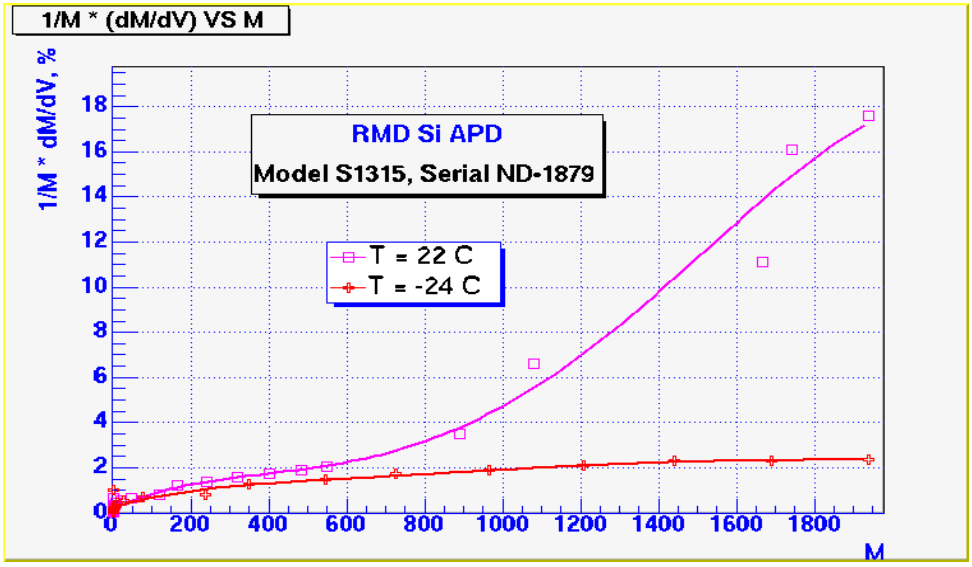

Figure 1-23 Derivative of fractional Gain with respect to HV vs. gain.

Operating the Crystals and their attached APD's at -24^0 C, motivated by the improved PWO performance at this temperature, thus also provides the ancillary benefit of considerably decreasing the dark current and improving the gain stability of the APD's.

1.10 Front End Electronics

The front end electronics consists of a preamplifier, located at the calorimeter, inside the warm bore of the detector solenoid, and a shaper amplifier outside the solenoid, in the movable counting house.

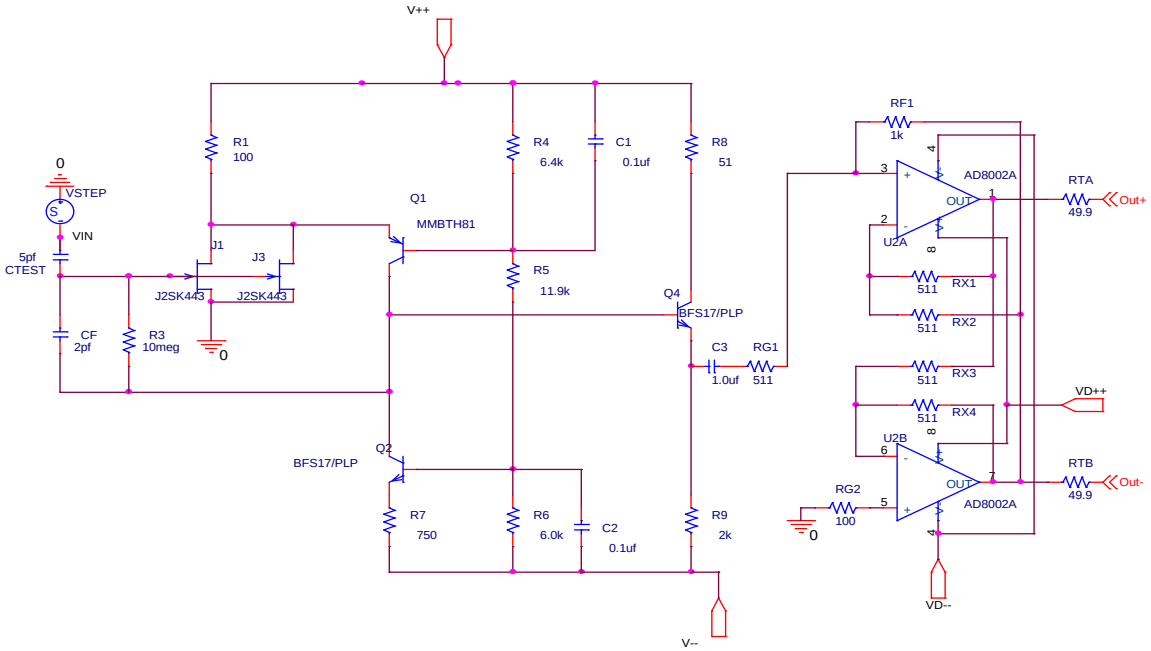

Figure 1-24: Circuit diagram for the preamplifier.

Figure 1-24 is an illustration of the Charge-Sensitive Preamplifier. This preamp utilizes a feedback capacitor CF and two field-effect transistors J1 & J3 at the input. The direct current feedback resistor R3 will determine the fall time of the output signal. The operating current of J1 & J3 is determined by the resistor R1, while the JFET characteristics determine the preamplifier's noise level and rise time.

The back end of the preamp is designed to drive differential cable (with a length of approximately 30m) in an effort to reduce the effects of EMI in the system. An added gain is achieved in this stage by a function of RF1/RG1. Figure 1-25 below shows the differential outputs of the Charge-Sensitive Preamplifier.

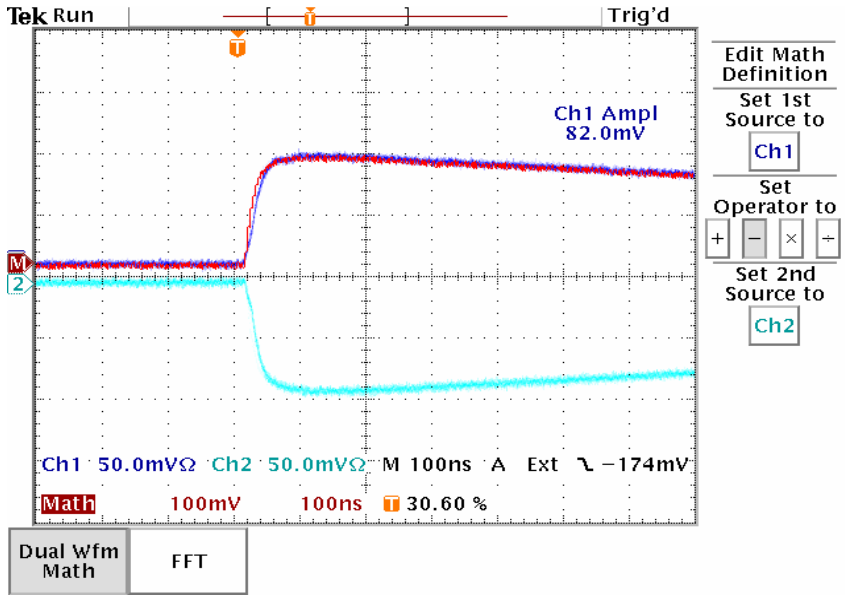

Figure 1-25: Output of the preamplifier.

Figure 1-26 is a photograph of a Crystal, with two APD's sitting next to it and a preamplifier box, with 2 preamps and a high-voltage filter, in its approximate location behind it.

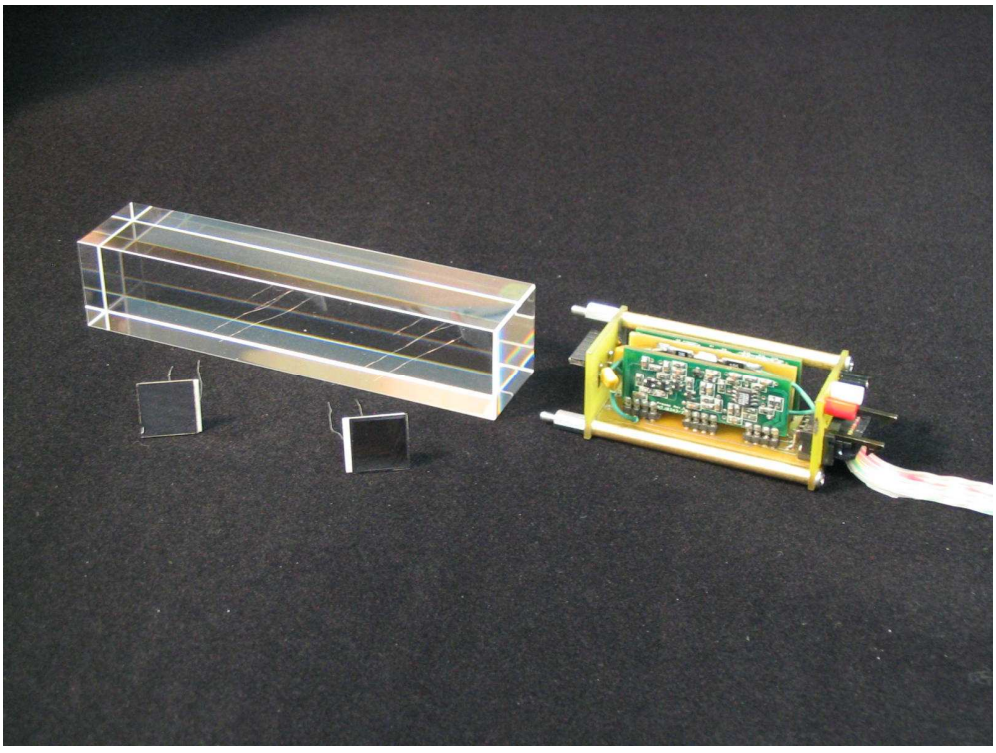

Figure 1-26: PWO crystal, 2 APD's and a preamplifier box.

Figure 1-27 is an illustration of the shaper circuit. This circuit utilizes a differential receiver at the input to accept the output of the preamplifier. The signal is then applied to a Sallen-Key filter for pass-band shaping purposes. Capacitor C3 is selected to be 2x the value of C4 which determines the fall time

constant of the output signal. A differential driver is used at the output stage as the signal is once again applied to twisted pair cable. The differential output of the shaper circuit can be observed in Figure 1-28. An additional output is also provided for summing into an analog trigger tower.

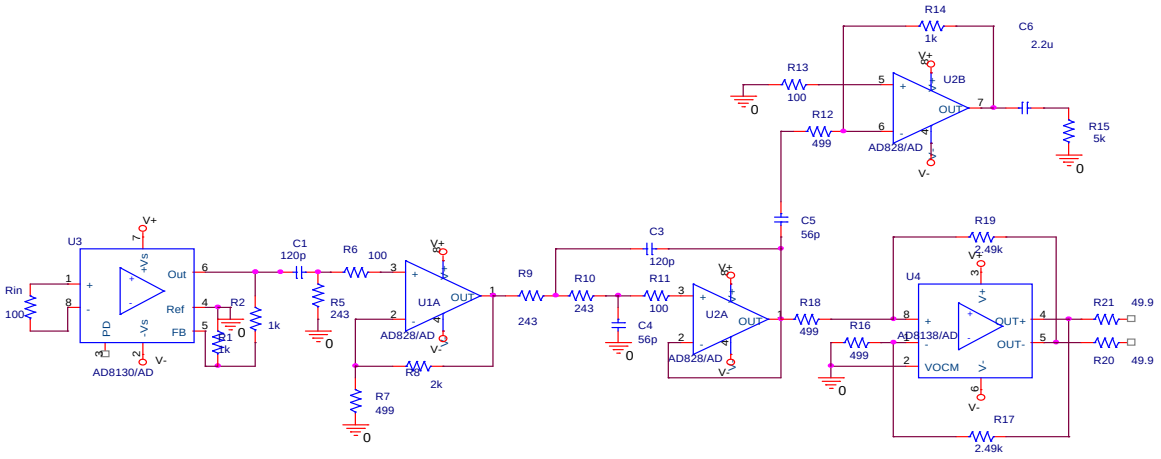

Figure 1-27. Circuit diagram for the shaper - amplifier.

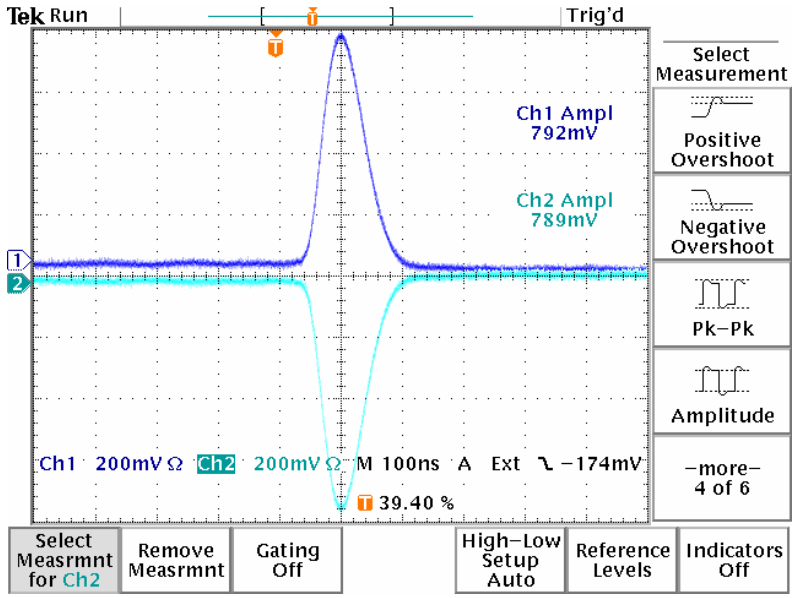

Figure 1-28. Output signal of the shaper circuit.

Finally, Figure 1-29 is a photograph illustrating a 9 crystal assembly of PWO crystals, APD's and preamplifiers for laboratory bench tests at NYU.

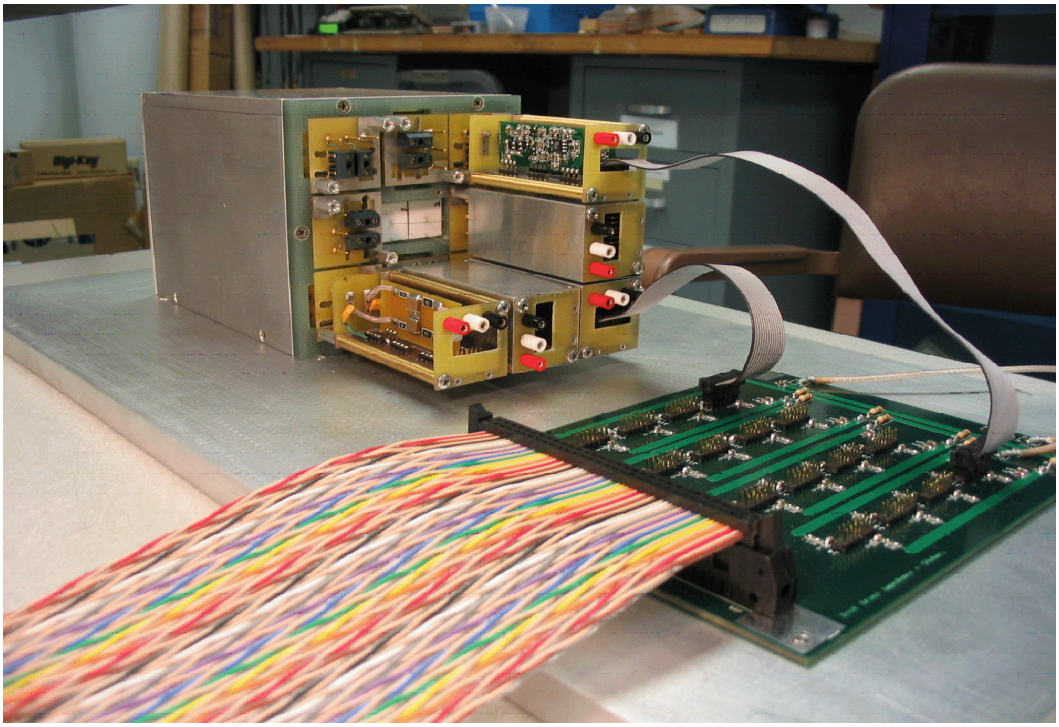

Figure 1-29. A 9-crystal assembly showing the box containing the 9 crystals plus APD's and 5 attached preamp boxes.

1.11 Cosmic Ray Muon Tests

Cosmic ray bench tests were performed at NYU {meco126} on a single PWO crystal read out by two avalanche photodiodes. The tests were done on a 3cm x 3cm x 14cm crystal from Bogoroditsk Co. This crystal size is different than our present design parameters of 3.75 x 3.75 x 12cm. It was wrapped in a Tyvek reflector on all sides. The photodetectors were 13mm x 13mm RMD model S1315 APD's. The test setup is shown schematically in Figure 1-30. The preamplifier amplifier system was the prototype described in the previous section. The detector was housed in a copper heat sink heat insulated inside a Styrofoam picnic box, and cooled to the temperature -23^{o} C by a JULABO Model F32 chiller with ethanol as the recirculating fluid.

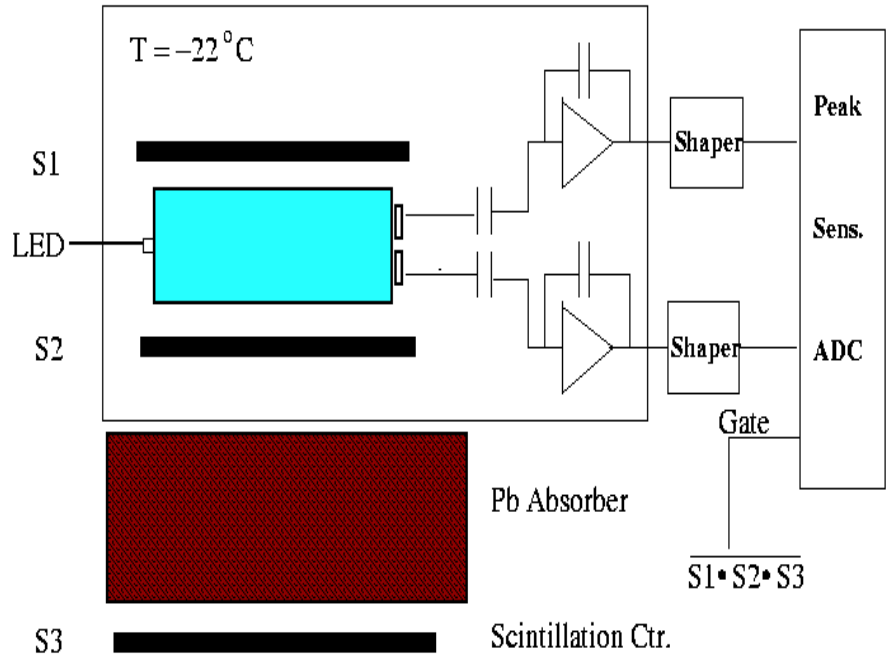

Figure 1-30. Schematic diagram of cosmic ray test setup.

Figure 1-31 is a photograph of a PWO Crystal with two APD's. With the present design parameters, the APD's would fit on the crystal face with no overhang.

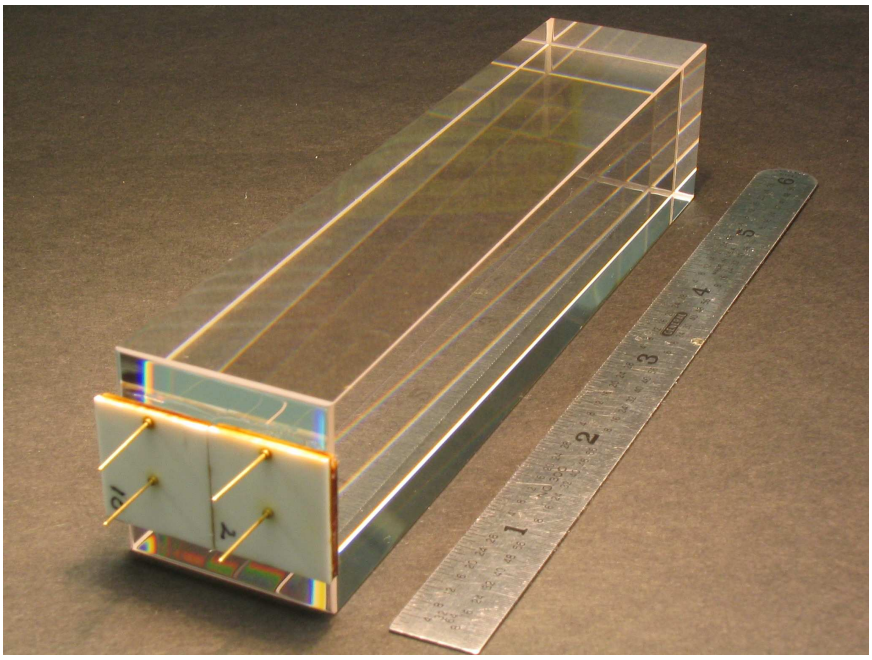

Figure 1-31. PWO crystal with two APD's.

The expected most probable energy deposition for a minimum-ionizing particle in the PWO crystal is 35MeV. The observed cosmic ray muon spectrum in the 2 APD's is shown in Figure 1-32 and is a reasonable fit to a Landau distribution.

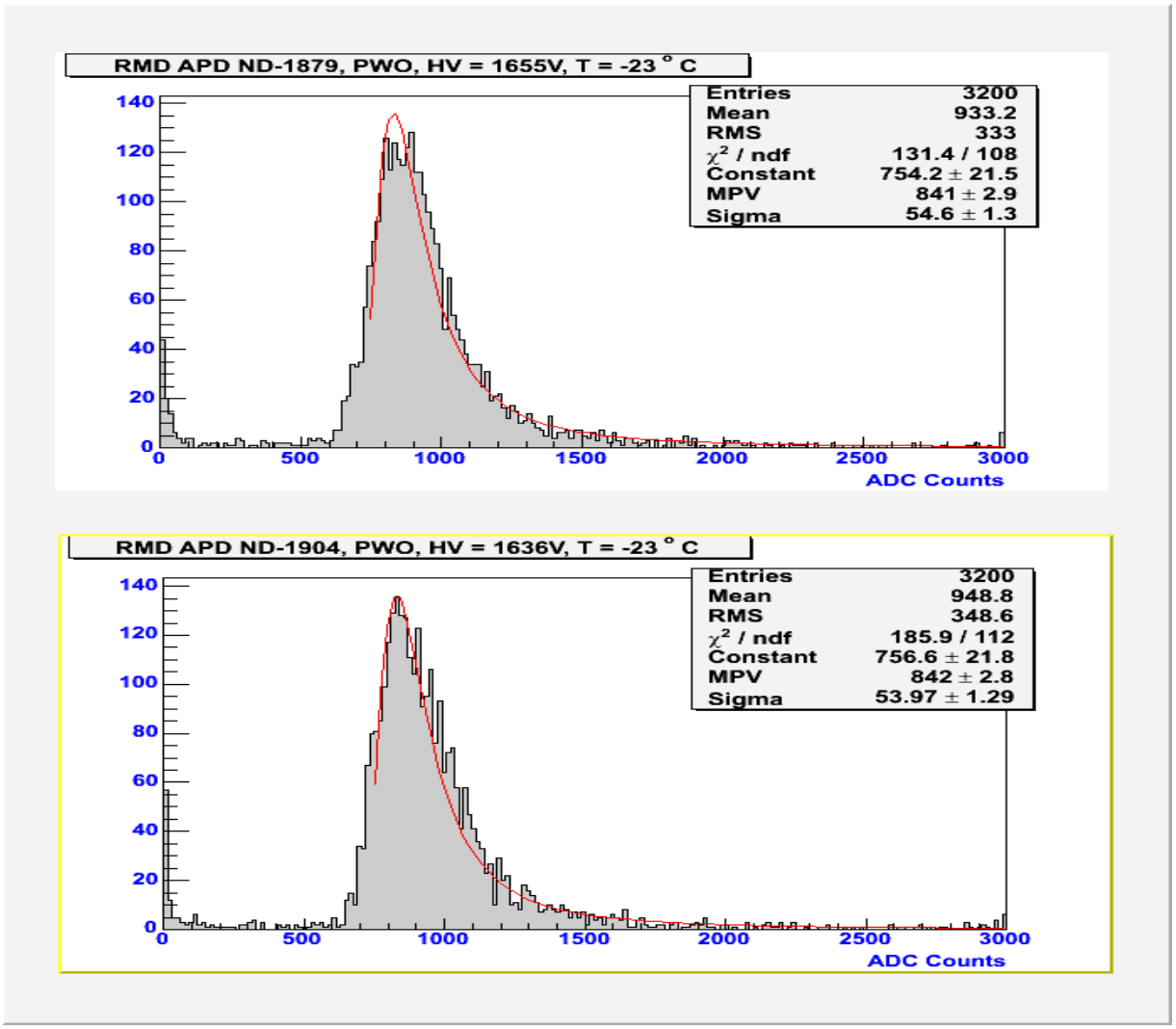

Figure 1-32. Typical cosmic muons spectra for APDs. The superimposed curves are fits to the data assuming a Landau distribution.

Running at an APD gain set at 300, with a 100 ns shaping time the measurements yielded an estimate for the collected photoelectron yield of 30 p.e./MeV and 18p.e./MeV for the two APD's, for an average yield of 24p.e./ MeV/APD. With a 50ns shaper the yields were 16 p.e./MeV and 22p.e. /MeV for an average yield of 19pe/MeV/APD. We translate this last number for the summed 2 APD signal to get a yield of 38 p.e. / MeV for the crystal

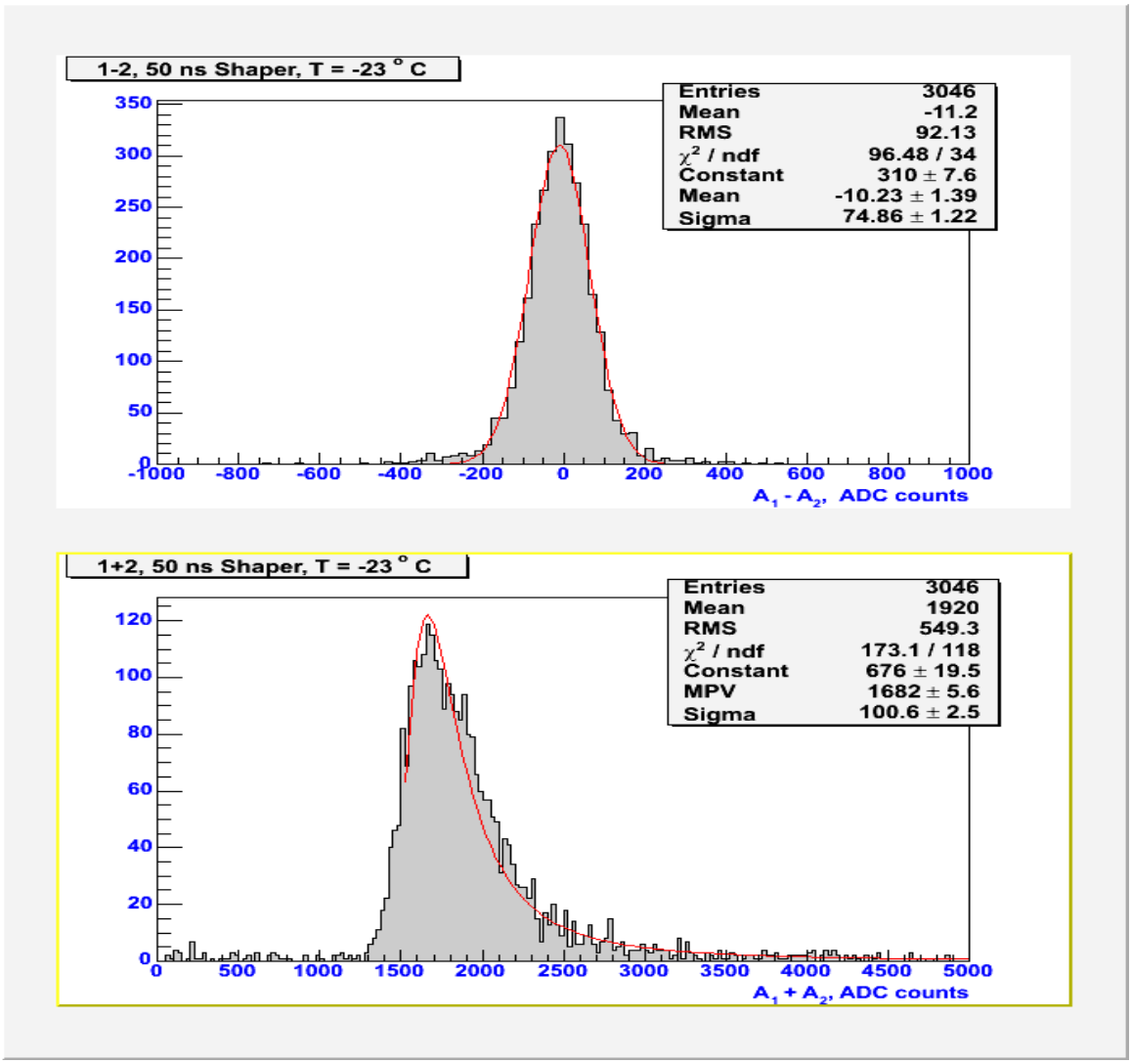

Figure 1-33. Histogram of the difference between two signals from APD's (upper plot) and of the sum of these two signals(lower plot). The top histogram is fit by a gaussian, the bottom one by a Landau distribution.

With two APD's collecting light from the same crystal, one can use them to separate out different contributions to the resolution. The distribution of the sum of the two APD signals has width contributions from Landau Fluctuations, photostatistics, and electronics noise, and is seen in Figure 1-33 (bottom) to have the expected Landau shape.

The distribution of the difference of the two signals, on the other hand, directly measures the summed contributions of photostatistics and electronics noise only, and is seen to have the expected Gaussian shape in Figure 1-33 (top). With the error on the sum and the difference of the two amplitude distributions the same, the σ of the difference distribution is exactly equal to the σ in the summed signal. The result for the combined contribution of photostatistics fluctuations and electronics noise to the measured fractional error ε in the summed 2-APD signal is:

$$\varepsilon = \frac{\sigma(A_1 - A_2)}{MPV(A_1 + A_2)} = \frac{74.86}{1682} \approx 4.4\%$$

From the measured photoelectron yield of 38 p.e./electron, above, we would predict, using an excess noise factor of F=2.2 for the APD, a photostatistics contribution of
$\sigma = \sqrt{F}/N_{PE} = \sqrt{2.2/(38 \cdot 35)} = 4.1\%$ at 35 MeV.
A direct measurement gave an average electronic noise of 3500 electrons/APD. This translates to a predicted electronic noise contribution, to the two APD sum, of $3500\sqrt{2}/(35 \cdot 38 \cdot 300) = 1.3\%$.
Summing these two predicted contributions in quadrature, we would get 4.3%, in satisfactory agreement with the measured 4.4%. Translating the resolution contributions to an MeV scale, we get measured results for the 35 MeV cosmic rays:

- σ(Electronic Noise) = 0.46 MeV
- σ(Photostatistics) = 1.44 MeV
- σ(E.N. & Photost) = 1.5 MeV
- Photoelectron yield = 38 p.e./MeV

All these results are for tests done with 3cm x 3cm transverse dimension crystals. For the chosen size of 3.75 cm x 3.75 cm, the result are expected to be somewhat degraded by a loss in light collection. The photoelectron yield and the electronic noise contribution to the resolution in MeV scale linearly with the collected light, while the photostatistics contribution scales as the square root of the colleced light. If the light collection were proportional to the ratio of APD active area to crystal face area, (a conservative assumption; it might vary somewhat slower because of the collection of reflected light) we would expect for the larger crystals (whose face area is 1.56 times that of the smaller ones), a photo-electron yield of 38 /1.56 =24 p.e./MeV. Summarizing the extrapolated results:

$$\sigma = \sqrt{F}/N_{PE} = \sqrt{2.2/(24 \cdot 35)} = 5.1\% \text{ at 35 MeV}$$

- σ(Electronic Noise) = 0.72 MeV
- σ(Photostatistics) = 1.79 MeV
- σ(E.N. & Photost) = 1.93 MeV
- Photoelectron yield = 24 p.e./MeV

Cosmic ray bench tests to measure these parameters directly for the 3.75 cm x 3.75 cm cross- section crystals are under way in the NYU laboratory.

1.12 Calibration and Monitoring

The calorimeter calibration system is designed to provide a determination of the absolute energy scale to 1 %, and provide channel-to-channel uniformity of 1 %.

The calorimeter serves as the triggering detector of the experiment. Since it is of no advantage to trigger on energies below those of signal electrons, the low energy tail of the calorimeter response to these electrons determines the trigger threshold of about 80 MeV measured energy. Uncertainties in calibration small compared to the calorimeter resolution (about 6 to 7 MeV) may, at worst, require a small decrease in the triggering energy threshold, with a corresponding increase in the background trigger rate. Uncertainties comparable to calorimeter resolution would cause more difficulties, however, and must therefore be avoided. For example, lowering the energy threshold at 80 MeV by 5 MeV causes an increase in the background trigger rate by about {meco052} a factor of 3.

If the level-zero trigger made with an analogue hardware sum of shaper amplifier trigger towers, the lowest gain cell will determine the threshold and therefore the trigger rate. Individual calorimeter cell gains should therefore be equalized at the hardware level to an accuracy of 1% determined by the

allowable hardware trigger rate. If, on the other hand, the lowest level trigger is made with digitized signals (an option being considered by the DAQ group), it would be sufficient to equalize the gains to about 10% at the hardware level, but the relative gains must still be known to 1% for a fast gain correction lookup table.

A higher level software trigger can then use the measured gains and energy deposition in individual cells to decrease the background trigger rate. In addition to being used for off-line analysis and on-line for the higher level trigger, the calibration data will therefore also be used to equalize cell gains at the hardware level.

Sources of small continuous variation such as electronic drifts or radiation damage require periodic changes to equalize gain. Short time scale variations, such as those due to temperature fluctuations within the boundaries set by hardware temperature control, give an irreducible source of variation which will necessitate some lowering of the hardware trigger threshold compared to what would be possible if only calorimeter resolution were involved.

Possible sources of short and long term variation include crystal non-uniformity, inherent crystal to crystal variation, APD to APD variation, radiation damage to crystals or APD's, temperature variation affecting crystal light output, temperature variation affecting APD and other electronics, voltage fluctuation resulting in APD gain fluctuation, and drift in front end electronics.

A sample of $PbWO_4$ crystals has been tested with a ^{137}Cs 0.662 MeV gamma source giving a measured crystal non-uniformity (maximum to minimum gain difference) averaging 3.3%. The range for the crystals was 1.8 – 4.8%. Because the electrons will be showering in the crystal, this non-uniformity is not expected to present a problem. The largest crystal to crystal differences, which will be corrected for by setting APD voltages, was 11% in the sample tested.

Crystal light output variation with temperature is typically about 5% per degree C for the PbWO4 crystals at -24^0 C ({Lecoq:1995}{Chen:1998}). APD temperature variation is 2.5 – 3.5% per degree C. Maintaining crystal temperature to about ± 0.1 °C, without doing temperature dependent corrections, will be sufficient to prevent resolution degradation or trigger rate fluctuations from this source. The APDs operate at about 1700V with gain changes of about 2% per volt. This requires voltage control and monitoring to a few tenths of a volt.

Radiation damage (described in 0), if any, or other radiation induced changes to either the PbWO4 crystals or the APD's will be occurring on very slow time scales, over periods of months. Therefore the tracking and adjustment of relative gains and of the absolute gain calibration will be sufficient to handle any associated changes of response.

The calibration system is designed to measure absolute gain and cell to cell variation, to measure periodically and tune the system hardware for long term variations, and to measure short time scale fluctuations to allow off-line corrections not possible on-line. Voltage and temperature control, although not part of the calibration system per se, are necessary to keep fluctuations to within levels that can be handled by calibration.

The absolute gain of the APD's as a function of voltage, and the response, including temperature dependence, of individual crystal APD assemblies will be tested prior to assembly of the calorimeter. These tests, which will provide a "pedigree" accompanying every assembly, will be done using radioactive sources, pulsed blue LED's, and cosmic rays.

For a cosmic ray measurement, a 3 x 3 array of crystals pointing horizontally upward will be sandwiched between two scintillation counters. The expected rate of cosmic rays going through a crystal is to be about 3 per minute for the laboratory calibration. Landau fluctuations, electronic noise and photo-electron statistics for the most probable minimum ionizing signal of 44 MeV, give a resolution of approximately 6 MeV. Collecting 1000 events in 3 hours would determine the position of the Landau peak to about ½ %.

To determine the detailed response of the calorimeter to electromagnetic showers, a 25 crystal (5 x 5) prototype calorimeter with exactly the same cell configuration as the final one, will be tested in laser backscattered gamma beam, at about 200MeV, at BNL's Electron Synchrotron Facility.

The APD voltages will be set according to measured cell gains to equalize gains at the start of the experiment. The original measurements will also be used to set the initial signal to energy conversion.

The preamp system is designed so that charge will regularly be injected at the front end in order to calibrate the full front-end electronics system. The system described below will thus allow measurement crystal and APD variation.

Gain changes of the APD's can be monitored with periodic calibration of individual crystal-APD cells. The experimental geometry constrains us to a system that injects light into the instrumented end of the crystal. Currently, laser, LED, or Xenon flasher systems which feed light in from the electronics end of the crystal are all either in use or planned for various experiments {BABAR:1995}{Ghio:1998}{ALICE:1999}{CMS:1997}. We are studying what is most appropriate for our case. The method will be tested by comparing results from such a system with the original, outside MECO cell calibrations, prior to exposure to beam.

Absolute energy calibration, can be provided by measuring the response of upstream calorimeter cells to electrons above 80 MeV, whose energy is measured by the tracker. The energy conversion for the back part of the calorimeter, which is less often hit by these electrons, can then be determined from the relative calibrations. If necessary, the magnetic field can be lowered in the detector region to provide a beam of higher intensity lower energy electrons which will go through the tracker and calorimeter. Stated differently, these tests provide a cross-calibration between the tracker momentum and the calorimeter energy.

It may be possible to provide an absolute energy calibration *in situ* with cosmic rays. The rates will be low. Inventing a practical trigger for this calibration, perhaps using part of the cosmic ray veto, may be non-trivial. Monte Carlo studies and bench tests are planned to determine the signal distribution and therefore the calibration precision that can be obtained with cosmic rays.

There will thus be at least two almost independent systems to monitor gain of most of the calorimeter. Individual cell changes will be tracked with a flasher system which can very quickly calibrate each cell and be used at frequent intervals. Less frequent absolute gain measurements can then be compared with the compounded results from the flasher system measurements to study the systematics involved. The gains of cells near the back of the calorimeter, for which only the flasher system and perhaps cosmic rays are available, will then be corrected if necessary. The symmetries of the detector may also be exploited. APD voltages will be periodically tuned to keep the hardware threshold constant to about one or two MeV.

Individual cell temperatures will be monitored by temperature sensors connected to the back of the crystal (see for example the Rugby Ball used in GRAAL {Castoldi:1998}). Once a trigger occurs, the measured gain versus temperature curves could be used on each event, if needed, to recalculate the total energy deposited in the calorimeter.

1.13 Calorimeter Cooling

The calorimeter has to operate at a stable temperature of -24^0 C for both crystals and APD's. As discussed above, the low temperature operation increases the photon yield of the crystals and decreases the dark current of the APD's.

The crystal and APD region of each vane is enclosed in a copper heat sink, part of the vane enclosure. As illustrated in the schematic diagram (Figure 1-34) and in the photograph (Figure 1-35) of an example from the test setup at the NYU laboratory, this heat sink has cooling coils welded to it. A continuous loop cooling-circuit, with circulating liquid, consists of a Chiller unit at the movable counting house outside the detector solenoid, with long, insulated cooling lines passing through the Instrumentation Feedthrough Bulkhead (IFB) and continuing to the calorimeter where they connect to the cooling coils. The needed length of insulated line will be approximately 25m. The temperature derivative of the PWO crystal light yield is of order 5%/degree C. Our experience in the NYU tests with a Julabo chiller and ethanol as the circulating fluid shows that the temperature is stable to better than 0.1^0 C in such a system. At this level of stability, we expect that no event-by-event temperature correction will be needed, although continuous temperature monitoring of the crystals and APD's will be important.

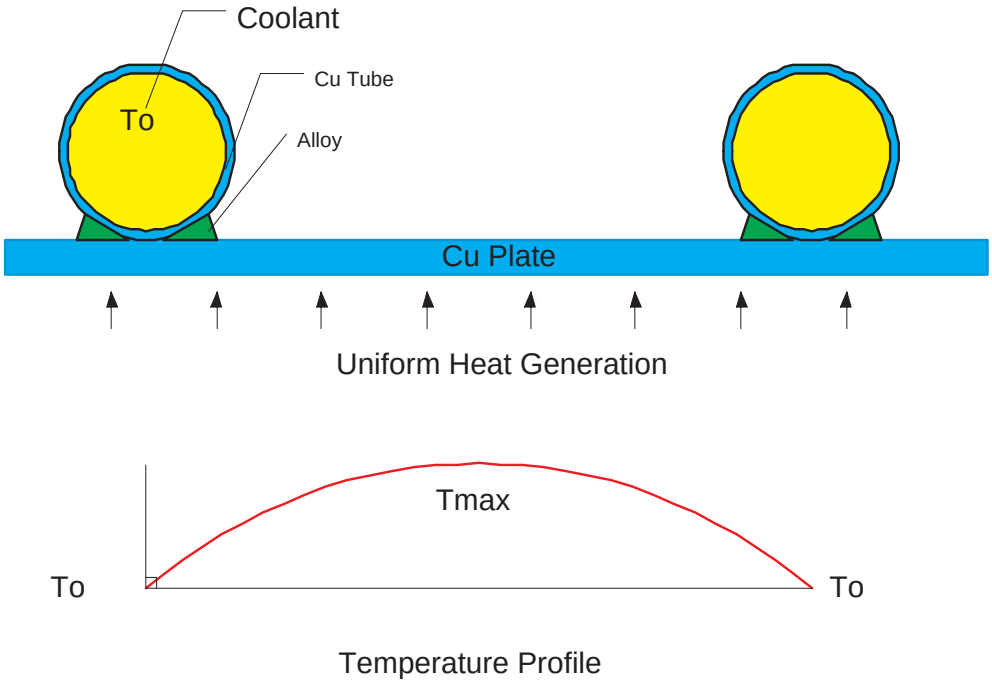

Figure 1-34 Cooling and heat sink schematic diagram.

Figure 1-35 Heat sink box with cooling coils from NYU laboratory tests**.**

With a dark-current of the order of order 10 nA at an APD bias voltage of order 2 KV, the dissipation is about 20 μW per APD, or a negligible 10 mW/vane. The heat load on the chillers will be dominated by the line losses. The heat transfer from the heat sink box to the individual crystals and APD's will be quite inefficient in vacuum, so that we expect long cooling-down times. The cool-down in vacuum will be measured during the prototype testing.

The preamps, with a dissipation ~ 200mW per channel, will be enclosed in their own copper heat sink box, and will operate at a nominal temperature of -24^0 C, the same as the crystals, with no stringent stability needs. Their total dissipation of ~120W per vane will be extracted by a separate outside chiller, so that fluctuations in the preamp system temperature will be decoupled from the crystal-APD temperature.

Inside the preamp enclosure the individual preamp ground shields will be "heat-shorted" to the heat sink box. The efficacy of this conduction cooling of the preamp components in the vacuum will be measured during our prototype testing. We will also look into any existing experience by others in running preamps in a vacuum. If the conduction cooling turns out insufficient to keep components at a reasonable temperature, one could consider a gas enclosure for the preamp system. However, this would be a serious complication for the mechanical construction of the vanes.

1.14 Mechanical Support

The four calorimeter **Vanes** are built as identical, completely independent units. No customization is made for the four different orientations of the 4 vanes, at their 3, 6, 9, and 12 o'clock positions. Each Vane is housed in a Vane Enclosure that provides the support frame and the cooling envelope for the PWO crystals and their readout.

Inside the Vane Enclosure, the 256 crystals are individually located and supported by a square-cell honeycomb of carbon-epoxy composite laminate (~0.2mm wall thickness), a section of which is shown conceptually in Figure 1-36. A similar carbon laminate structure is being used by CMS and ALICE for their PWO calorimeters. The honeycomb strength allows a structure to be built whose dead material is only 0.3% of the active mass of the calorimeter. The square honeycomb structure is contained in, and attached to, the metal box that forms the vane enclosure as well as the heat sink for cooling the detectors.

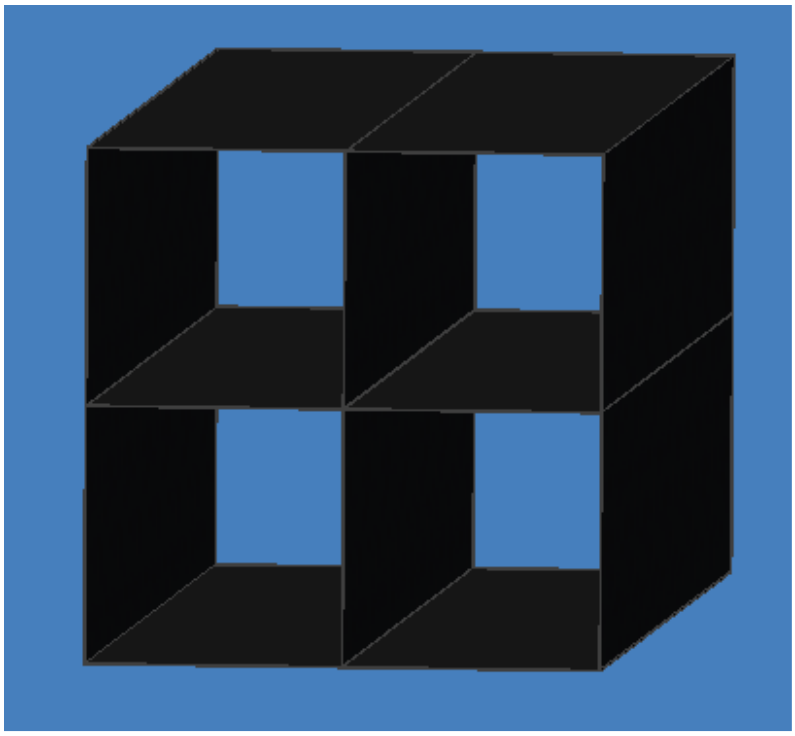

Figure 1-36 Conceptual idea of honeycomb cell-support structure.

The vane enclosure, shown schematically in Figure 1-37, has a separate compartment for the crystals with their APD readouts and for the preamplifier system connected to them. The two compartments are separated by a copper-G10-copper wall, perforated to allow connecting the APD's to the preamps and high voltage. The vane enclosure has thin (~2mm Cu) wall at the electron entry face, moderate thickness walls (~1cm) on 4 other faces in the active region for detected electrons, and a thick (~3cm) wall, performing as the attachment plate at the outermost radius, which is outside the region of relevant electron orbits.

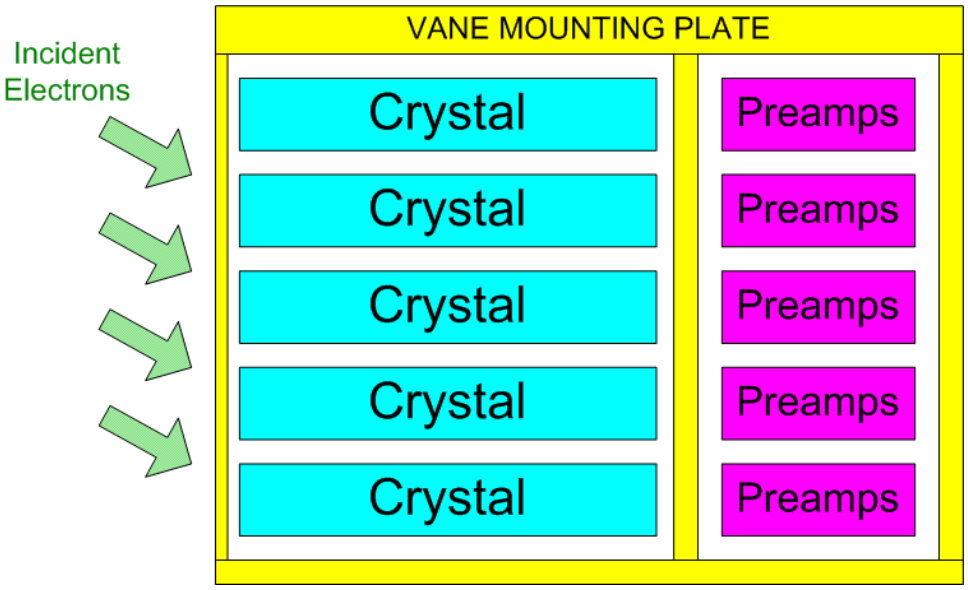

Figure 1-37: Vane enclosure schematic.

Each of the 4 Vanes of the Crystal Calorimeter is attached to a rigid rolling **Detector Cage,** kept entirely outside the detector region's maximum radius (Figure 1-38), by the attachment plate at the outer edge of the vane. Vernier positioning devices are part of this attachment to allow centering the calorimeter on the axis to better then 1 mm. The Detector Cage serves as a rigid mount for the calorimeter and for rolling it in and out of the cryostat on rails attached to the inner wall of the cryostat, for installation and for servicing. The Detector Cage is part of, and defined in, the detector support structure (WBS 1.3.4.8) in the Muon Beam Line.

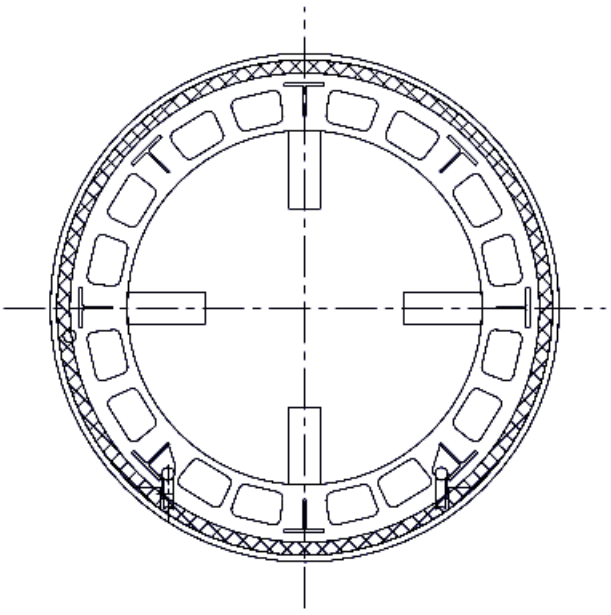

Figure 1-38 Calorimeter detector cage.

1.15 Conclusion

Summarizing, the proposed crystal calorimeter provides a trigger for the experiment, including a reference time t_0 for the tracker drift-time digitizing. It sharpens the event signature by adding to the precision measurement of the electron momentum in the tracker, a lower resolution, but independent measurement of the electron's energy and of an (x,y,z)-coordinate on its trajectory. The high-energy threshold made possible by the good resolution of about 7 MeV for a super-cell results in a low trigger rate and a small final data sample. A level 1 trigger rate of order 1Khz appears practical.

References added:

Lorenz:1986
E. Lorenz, G. Mageras, and H. Vogel, NIM A249, 235 (1986)

Kubota:1992
Y. Kubota et. al., NIM A320, 66 (1992)

Barlow
R.J. Barlow et. al., Technical Report No. 7887, SLAC (unpublished) SLAC-PUB-7887

Kampert:1994
K.H. Kampert et. al., NIM A349, 81 (1994)

Lecoq:1995
P. Lecoq et.al. NIM A365, 291 (1995)

Hall:1990
G. Hall in Proceedings of the Large Hadron Collider Workshop {CERN- PUB,1990} vol.3 p. 693
CERN 90-10 (ECFA 90-133)

Singer:1974
P. Singer, Springer Tracts in Modern Physics, **71**, 39 (1974)

Mukhopadhyay:1977
N. Mukhopodhyay, Rep. Prog. Phys. **30**, 1, 1977

Annekov:1997
A. Annekov et.al., CMS Note, CERN (unpublished), CMS 1997/055

Chen:1998
H.F. Chen et.al., NIM A414, 149 (1998)

Annekov:1999
A. Annekov et.al., NIM A426, 486 (1999)

Baccaro
S. Baccaro et.al. CMS Note 030, CERN (unpublished)

Borchi:1994
E. Borchi and M. Bruzzi, Riv. Del Nuovi Cimento **17**, N11 (1994)

Moll:1999
M. Moll, E. Fretwurst, and G. Lindstrom, NIM A426, 87 (1999)

Bosetti:1994
M. Bosetti et.al., NIM A343, (435) 1994

Auffray
E. Auffray et.al., CMS Note 038, CERN (unpublished)

BABAR:1995
BaBar Collaboration, Technical Design Report for the Babar Detector (1995).

Ghio:1998
F. Ghio, et. al. NIM A404, 71 (1998)

ALICE:1999
ALICE, Technical Design Report No. 99-4, CERN (unpublished) CERN-LHCC 99-4 (1999).

CMS:1997
CMS, Technical Design Report No. 97-33, CERN (unpublished) CERN-LHCC 97-33 (1997).

Castoldi:1998
M. Castoldi, et.al., NIM A403, 22 (1998)